Beyond Static Screens: A High-Throughput Pooled Imaging CRISPR Platform for Dynamic Phenotype Discovery

Sravasti Mukherjee[1,2,8], Menno van Tooren[3], Giulia Zanetti[1,8], Dimitris Sfakianakis[4], Dominique Kemps[5], Jeffrey Klarenbeek[6,8], Hendrik J. Kuiken[7], Cor Lieftink[7], Bram van den Broek[1,6,8], Roderick L. Beijerbergen[7,8], Kees Jalink[1,2,8]

1. Division of Cell Biology, The Netherlands Cancer Institute, Plesmanlaan 121, 1066CX, Amsterdam, The Netherlands
2. Swammerdam Institute of Life Sciences, University of Amsterdam, Science Park 904, 1098XH, Amsterdam, The Netherlands
3. Princess Máxima Center for Pediatric Oncology, Heidelberglaan 25, 3584CS, Utrecht, The Netherlands
4. Academic Medical Centre, Meibergdreef 9, 1105AZ, Amsterdam, The Netherlands
5. Wageningen University and Research, Droevendaalsesteeg 4, 6708PB, Wageningen, The Netherlands
6. Bioimaging Facility, The Netherlands Cancer Institute, Plesmanlaan 121, Amsterdam, 1066CX, The Netherlands
7. Division of Molecular Carcinogenesis, The NKI Robotics and Screening Center, The Netherlands Cancer Institute, Plesmanlaan 121, 1066CX, Amsterdam, The Netherlands
8. Van Leeuwenhoek Centre for Advanced Microscopy (LCAM), Amsterdam, The Netherlands

ABSTRACT

Understanding the dynamic regulation of signaling pathways requires methods that capture cellular responses in real time. While high-content imaging-based genetic screens have transformed functional genomics, they have remained largely limited to static or binary phenotypes. Here, we present DynaScreen, an imaging-based, pooled CRISPR screening platform that enables high-throughput investigation of dynamic cellular phenotypes at single-cell resolution. By integrating Förster resonance energy transfer (FRET)-fluorescence lifetime imaging microscopy (FLIM) biosensors with photoactivation-based single-cell tagging and pooled CRISPR screening technology, we establish a scalable system to identify genes that regulate the timing, amplitude, and duration of signaling responses.

As proof of principle, we applied this approach to the cAMP signaling pathway, a key regulator of cellular physiology. Using a custom guide RNA (gRNA) library, we tracked real-time cAMP dynamics in response to agonist stimulation and identified genes that modulate its basal levels and response kinetics. Cells with aberrant signaling were selectively photoactivated, isolated by fluorescence-activated cell sorting (FACS), and subjected to next-generation sequencing to pinpoint causal genetic perturbations. This strategy successfully uncovered known and novel regulators of cAMP dynamics.

In conclusion, the integration of FLIM microscopy, CRISPR technology and open-source software to handle image analysis, automated hit identification and data representation, enables real-time exploration of dynamic phenotypes in a wide range of biological settings.

INTRODUCTION

Genetic screens enable the dissection of gene function by linking targeted perturbations to observable phenotypes. There are two main types: arrayed screens in multi-well plates, and pooled screens. In arrayed screens, each well hosts a distinct genetic perturbation, allowing direct observation of its phenotypic effects. While highly informative, these screens are labor-intensive, expensive, and difficult to scale—especially when phenotype recording and detection are time-consuming. By contrast, pooled screens enable many genes to be targeted simultaneously within a single culture dish, with each cell receiving a perturbation in only one specific gene (Bock *et al*, 2022). A major advantage of pooled screens is that all cells grow at the same culture conditions, receive the exact same treatment and are analysed in parallel. This eliminates variability due to growth medium evaporation, cell aging, confluence and day-to-day fluctuations that often hamper arrayed screens (Kim *et al*, 2024). In pooled screens for genes that affect cellular fitness, hits can be readily identified by massive-parallel sequencing. To identify genes involved in phenotypes that do not affect cellular fitness, fluorescence-activated cell sorting (FACS) and imaging-based screens have been instrumental (Walton *et al*, 2022) (Fig. 1A).

Imaging-based screens leverage advanced microscopy techniques to enable unbiased, high-throughput assessment of essentially any phenotype discernable by light microscopy, including proliferation, differentiation, morphological changes, and immune responses. However, in pooled screens and in the absence of an effect on cellular fitness, the genes involved in a phenotype of interest cannot be identified by high-throughput sequencing; instead such experiments require elaborate decoding of genotype-phenotype relationships, e.g. by Fluorescence In Situ Hybridization (FISH), In Situ Sequencing (ISS) or rolling circle amplification (Feldman *et al*, 2019; Wang *et al*, 2019). Recent landmark innovations—including photoactivation tagging (Photostick), microraft arrays, and automated cell selection platforms—have expanded pooled screening capabilities (Hasle *et al*, 2020; Piatkevich *et al*, 2018; Wheeler *et al*, 2020; Yan *et al*, 2021).

Nevertheless, these studies have largely focused on phenotypes that are static or binary in nature – such as altered cell morphology, protein expression, cell viability or nuclear translocation (Kanfer *et al*, 2021; Yan *et al*, 2021; Lawson *et al*, 2017; Hasle *et al*, 2020; Wheeler *et al*, 2020). Understanding the complexity of cellular signals and behavior requires assays that capture the temporal progression of events. For example, in both the ERK signaling pathway and neuronal Ca^{2+} signaling, it is well established that the biological outcome of sustained signals is distinct from oscillatory ones when looking at cell fates (Albeck *et al*, 2013; Kawaguchi *et al*, 2011).

In our lab, we study the dynamics of temporal changes in the second messenger cyclic adenosine monophospate (cAMP) at the single-cell level. cAMP is a crucial regulator of diverse cellular functions, including metabolism, gene expression, and differentiation. cAMP signaling is triggered when agonists bind to G-protein coupled receptors (GPCRs) that activate the G protein $G_{\alpha s}$ (Fig. 1B (i)). $G_{\alpha s}$ acts as a molecular switch which, in turn, activates Adenylate Cyclase (AC), the enzyme that generates cAMP from adenosine triphosphate (ATP). In humans, ACs comprise a diverse family of 10 isozymes that differ in subcellular localization, activity as well as in crosstalk with other second messengers (Li *et al*, 2024). Over time, cAMP levels return towards baseline (basal levels) due to the activity of phosphodiesterases (PDEs), which catalyze conversion of cAMP to adenosine monophosphate (AMP). Again, the intricate regulation of this pathway is implied by the existence of no less than 40 different PDEs and splicing variants, which derive from 10 families encoded by 21 individual genes (Azevedo *et al*, 2014). As with ERK and Ca^{2+}, the dynamics of cAMP signals matter. Transient cAMP-spikes rapidly activate the effector Protein Kinase A

(PKA) to regulate acute responses such as glucose metabolism in hepatocytes, whereas sustained cAMP elevation drives long-term effects like neuronal differentiation via cAMP response element-binding protein (CREB) activation (Inda *et al*, 2017). We are, however, only beginning to understand how cells encode information in cAMP dynamics at the single cell level (Fig. 1A, 1B (i), (ii)).

Key to understanding the dynamics of cAMP signals in single cells in real time was the development of advanced biosensors, such as the exchange protein activated by cAMP (Epac)-based Förster resonance energy transfer (FRET) sensors developed by us and others (Klarenbeek *et al*, 2015, 2011). We use fluorescence lifetime imaging microscopy (FLIM) to read out a dedicated FLIM-optimized Epac sensor quantitatively and with high temporal resolution. Thus, FRET-FLIM imaging provides a unique window into all temporal aspects of cAMP signaling: baseline levels, peak intensities, rise- and fall-times, and more (Mukherjee *et al*, 2024).

In a previous study, we demonstrated, for the first time, the feasibility of dynamic FRET-FLIM in an arrayed screen format (Harkes *et al*, 2021). By identifying the dominant factors that drive cAMP breakdown among a panel of 22 different PDEs, we demonstrated that signal amplitude, noise levels, drift, and speed of image analysis routines now allow for single-cell quantification of cAMP dynamics in a screening context. However, with assays that may take up to an hour per well, it is impossible to extend the scale of such screens beyond a few dozen genes. Here, we develop **DynaScreen**, capable of elucidating dynamic response phenotypes in large pools of cells each carrying a specific genetic perturbation.

In essence, time-lapse FLIM recordings are made from an agonist-stimulated, heterogeneous population of cells previously transduced with a pooled CRISPR library. That is followed by automated image-analysis of signaling dynamics at a single-cell level, and individual cells of interest are tagged by UV-photoconversion of a photoactivatable mCherry (PA-mCherry). Tagged cells are then isolated by FACS for subculture or identification of enriched guide RNA (gRNA) sequences. We provide a proof-of-principle using a gRNA library targeting 318 genes with 4 gRNAs per gene, and identify genes that affect baseline and agonist response kinetics of cAMP.

While currently optimized for analysis of FRET-FLIM signal dynamics, DynaScreen can be easily adapted to basically any dynamic phenotype, provided it is discernable by automated image analysis. Thus, DynaScreen is a versatile paradigm to extend pooled CRISPR screening beyond static endpoints, representing a major step forward in our ability to dissect gene function in the context of dynamic cellular responses.

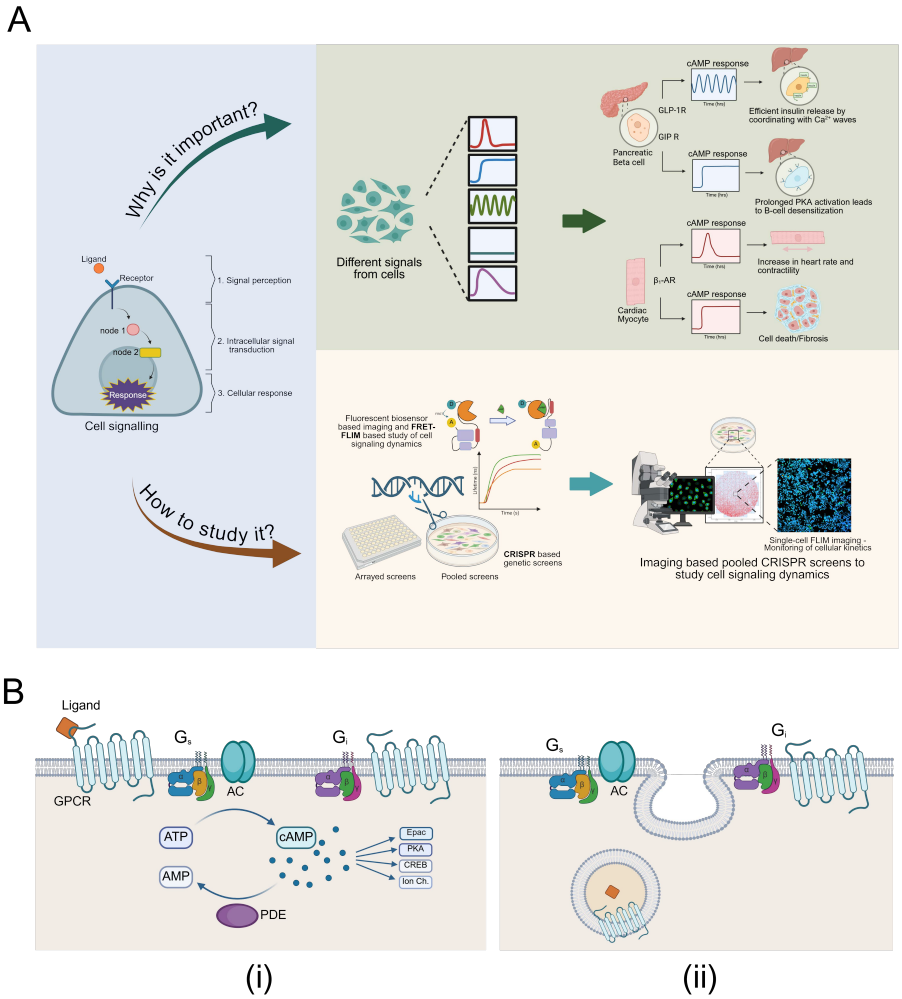

Fig. 1. Dynamics in cell signaling. (A) *Left pane shows how cell signaling leads to a response. Right upper pane shows that the outcome of signaling events does not depend solely on strength of second messenger signals, but also on the location and time course (dynamics) of signals. Examples in cAMP signaling include the differential outcome of oscillatory versus sustained cAMP signals in islets of Langerhans (Tian et al, 2011), and of transient versus sustained cAMP signals in cardiac cells (GLP-1R - Glucagon-Like Peptide-1 Receptor and GIP R - Glucose-dependent Insulinotropic Polypeptide Receptor). The right lower pane depicts analysis of cAMP dynamics by time-lapse FRET-FLIM imaging combined with CRISPR-Cas9 mediated genetic screens in large numbers of cells.* ***(B)*** *Depiction of the cAMP signaling cascade and factors that determine the signaling dynamics.* ***(i)*** *cAMP is generated by any of the 10 different Adenylate Cyclases (AC) in cells. ACs are activated via the G protein $G_{\alpha s}$ under control of specific GPCRs, and inhibited via $G_{\alpha i}$ following activation of another set of GPCRs. The balance of $G_{\alpha s}$ and $G_{\alpha i}$ determines cAMP synthesis. Once synthesized, cAMP activates a number of effector proteins including Protein Kinase a (PKA), cAMP Response Element (CREB), Exchange Protein directly affected by cAMP (Epac) and ion channels to exert cellular effects. cAMP breakdown is mediated by dozens of isoforms of phosphodiesterases (PDE) which stem from 11 gene families (Azevedo et al, 2014).* ***(ii)*** *Following activation by their cognate ligands, many GPCRs are phosphorylated and internalized. This often sequesters them away from the G protein and AC. The actual dynamic changes in cAMP concentration are determined by the balance between localized synthesis, breakdown and receptor inactivation, as well as by feedback mechanisms and interactions with other messenger cascades. Drawn is just a small part of the complexity of this signaling cascade.*

RESULTS

Pipeline for imaging based dynamic pooled screen

A schematic overview of the proposed screening pipeline is shown in Fig. 2. In brief, cells expressing the FLIM biosensor, a nucleus-targeted photoconvertible fluorescent tag, and a doxycyclin-inducible Cas9 (iCas9) are transduced with a lentiviral gRNA library and selected using puromycin. Time-lapse FLIM recordings are then made of large numbers of cells in parallel, and receptor agonists are pipetted in from concentrated stocks to induce a transient increase in cAMP. Data are then automatically analysed by an in-house developed FIJI routine, where first, cells are segmented using CellPose (Stringer *et al*, 2021; Pachitariu & Stringer, 2022), and then, the dynamic changes in each individual cell are quantified and visualized in a variety of manners. Next, cells with aberrant kinetics (hits) can be automatically selected using various criteria controlled by the experimenter, and the stage coordinates of all hits are provided as output. These coordinates allow the microscope to revisit hit cells and run a UV-photoactivation protocol to activate the cell tags. Tagged cells can then be isolated by FACS and analysed by next-generation sequencing (NGS) of the gRNAs.

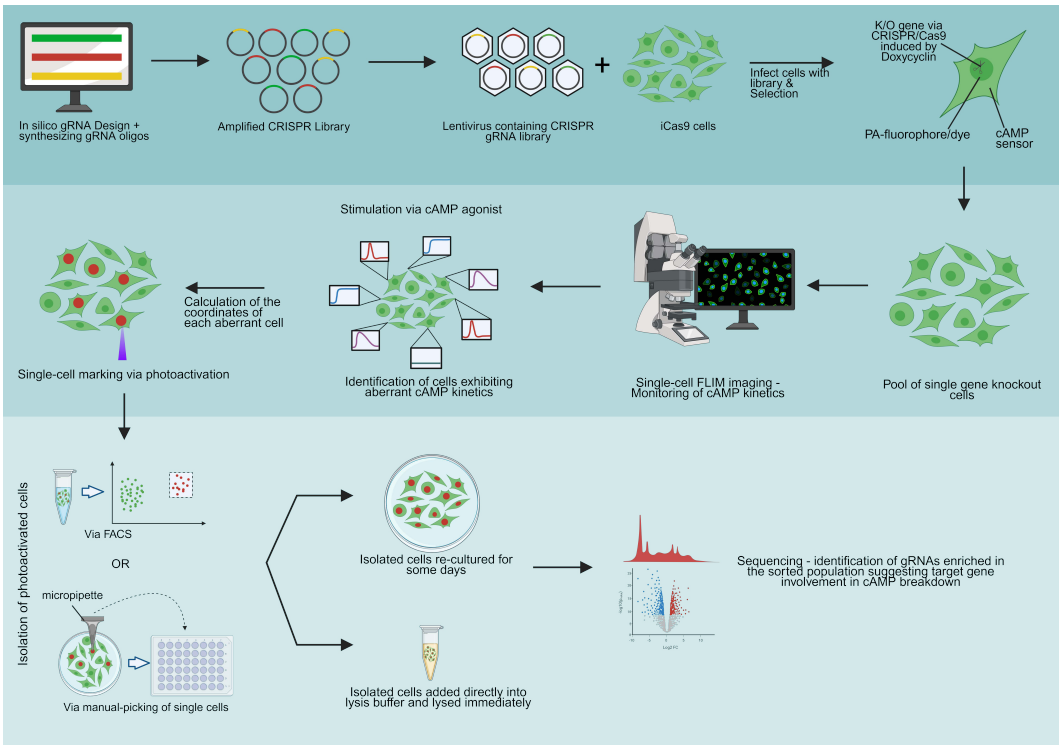

Fig. 2. Schematic overview of the pooled dynamic screening pipeline. *A dedicated CRISPR gRNA library, centered around genes known or suspected to affect cAMP signaling, is cloned in lentivirus and used to infect iCas9-expressing cells that also express the cAMP sensor and a photoactivatable fluorescent tag. Following selection of cells, editing is induced with doxycyclin to generate a pool of edited cells, each with a single gene knocked out. This pool of single gene knockout (KO) cells is screened by time-lapse FLIM microscopy and analysed for cells with aberrant cAMP dynamics (i.e. hits). The stage coordinates of each hit are used to revisit these cells so as to photoactivate the red fluorescent tag using UV light. After trypsinization, red cells can then be picked manually for confirmation, or sorted by FACS for NGS.*

Whereas the screens are carried out with a human gRNA library in HeLa (human cervical cancer) cells, initial technical characterization and optimization of all aspects of the pipeline was in Cos7 (green monkey kidney) cells (Supplemental Material 1, Fig. S1). We scrutinized the expression of reporter constructs (Fig. 3A, S1B), the precision and throughput of FLIM imaging (Supplemental Material 2), the automation of image analysis and hit selection, the activation of the photoinducible tags, isolation of hit cells by FACS, and the DNA isolation and sample processing for very low cell counts. Cells were selected for optimal expression of FLIM sensor and PA-mCherry as well as for high FRET span (baseline – calibration) and stable expression as shown in Fig. 3B and described in detail in Supplemental Material 1.

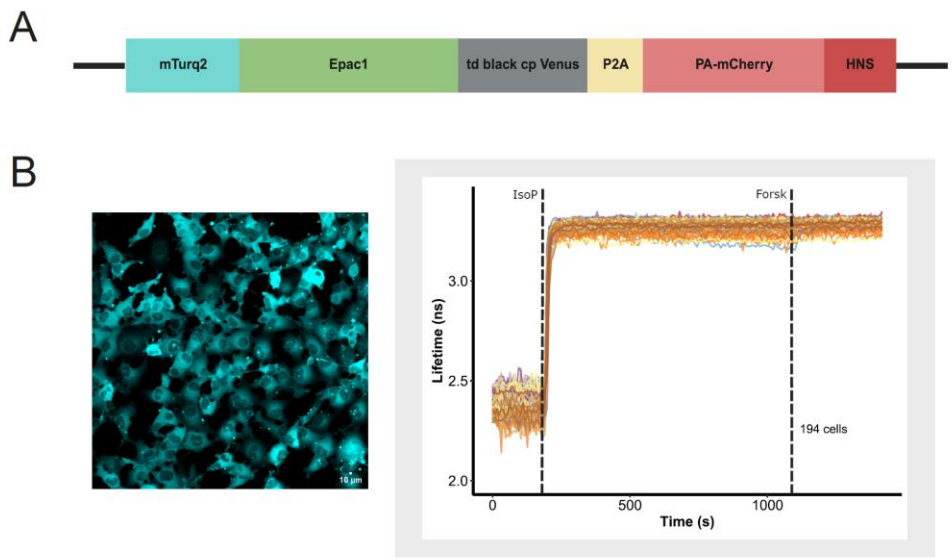

Fig. 3. Responses to isoproterenol and forskolin in Cos7 H250 cells detected by time-lapse FLIM. (A) *The reporter construct (H250) used to express the Epac1-based cAMP sensor and a nucleus-targeted photoactivatable mCherry at equal levels.* ***(B)*** *Left, Cos7 cells (Green Monkey kidney cells) expressing the reporter construct (H250). mTurquoise intensity is depicted in cyan. Right, cAMP responses in 194 individual cells. FRET span = ~0.8ns. Scale bar: 10 µm. IsoP denotes addition of isoproterenol; Forsk denotes addition of forskolin to directly activate AC and maximize the response. Note that raw FLIM data are shown, i.e. without normalization. Typical example out of > 40 repeats.*

FIJI script for automated analysis of FLIM traces and the identification of hits

To date, no software is available that can handle FLIM data in a screening context. To this end we developed FAST-HIPPOS: FLIM Analysis of Single-cell Traces for Hit Identification of Phenotypes in Pooled Optical Screening, a collection of macros in FIJI (Schindelin *et al*, 2012) to analyse time-lapse FLIM data and to automatically identify hit cells and subsequently drive their photoactivation (Fig. 4). The script can load time-lapse FLIM data directly from Leica .lif files, Lambert Instruments .fli files, as well as from exported (ome) .tiff files. Simple intensity data and ratio imaging data are also supported. Optional preprocessing steps include drift correction and bi-directional scanning phase mismatch correction.
Using these data, cell segmentation can be performed with CellPose in Fiji (https://github.com/BIOP/ijl-utilities-wrappers) on the summed-intensity projection of a subset or all of the time-lapse images (Fig.

4A). Based on the obtained segmentations, temporal lifetime traces are extracted for individual cells by intensity-weighted averaging the pixels belonging to each cell (Fig. 4B). Lifetime trace data can be represented in a variety of manners: as time traces graphs, tables, density graphs, kymographs and more. Optional outputs include (smoothed) lifetime-intensity overlay movies (Fig. 4A and Supplementary movie 1 and 2), (time-lapse) lifetime histograms, and (time-lapse) scatter plots of cell lifetimes against various parameters (Fig. 4C and Supplementary movie 3 and 4).
If applicable, the script can automatically determine the time points of stimulation and calibration based on steep inclines in the average trace, and can use this information to subdivide traces into 'baseline', 'response' and 'calibration' segments. The data from a user-selectable range of time frames can then be used to call hit cells through a multi-parameter scan of the data traces, with user-defined selection criteria, e.g. baseline lifetime, maximum response lifetime, average lifetime in a defined time range after stimulation or before calibration, etc. (Fig. 4D). Alternatively, hit cells can be selected graphically by simply drawing a ROI in time traces, sorted kymograph or the overlay movie (see Supplementary movie 5). The detected hits are displayed in a time traces graph, outlined on the lifetime-intensity overlay movie for inspection (Fig. 4E), and are shown in density graphs, kymographs and (dynamic) time-lapse histograms (Fig. 4F). In 'inspection mode', data of different graphs are visually coupled, i.e. clicking on a particular trace will highlight the corresponding cell and vice versa (Supplementary movie 6), enabling quick examination of the data.
The (X, Y) stage coordinates of hit cells are saved as Leica .rgn files, which can be directly imported into LAS X Navigator (Fig. 4G). Photoactivation is then performed using a static external UV laser aligned to the center of the microscope objective, with a spot size roughly equal to the size of a cell nucleus (8-10 µm), enabling single-cell activation without affecting neighboring cells.
For our screens, we imaged large regions (e.g., 200 tiles ~ 40,000 cells) without overlap. Image stitching is performed in FIJI to ensure correct pixel size to prevent image distortion and preserve stage coordinates.

To accelerate analysis, FAST-HIPPOS makes extensive use of GPU acceleration (Haase *et al*, 2020). A detailed description of the analysis pipeline and the script can be found at https://imagej.net/plugins/fast-hippos. The script is instrumental for automating the analysis of FLIM screens, but in general should also be well-suited for inspection and analysis of multi-cell time trace data, for FLIM, ratio data and intensity data alike.

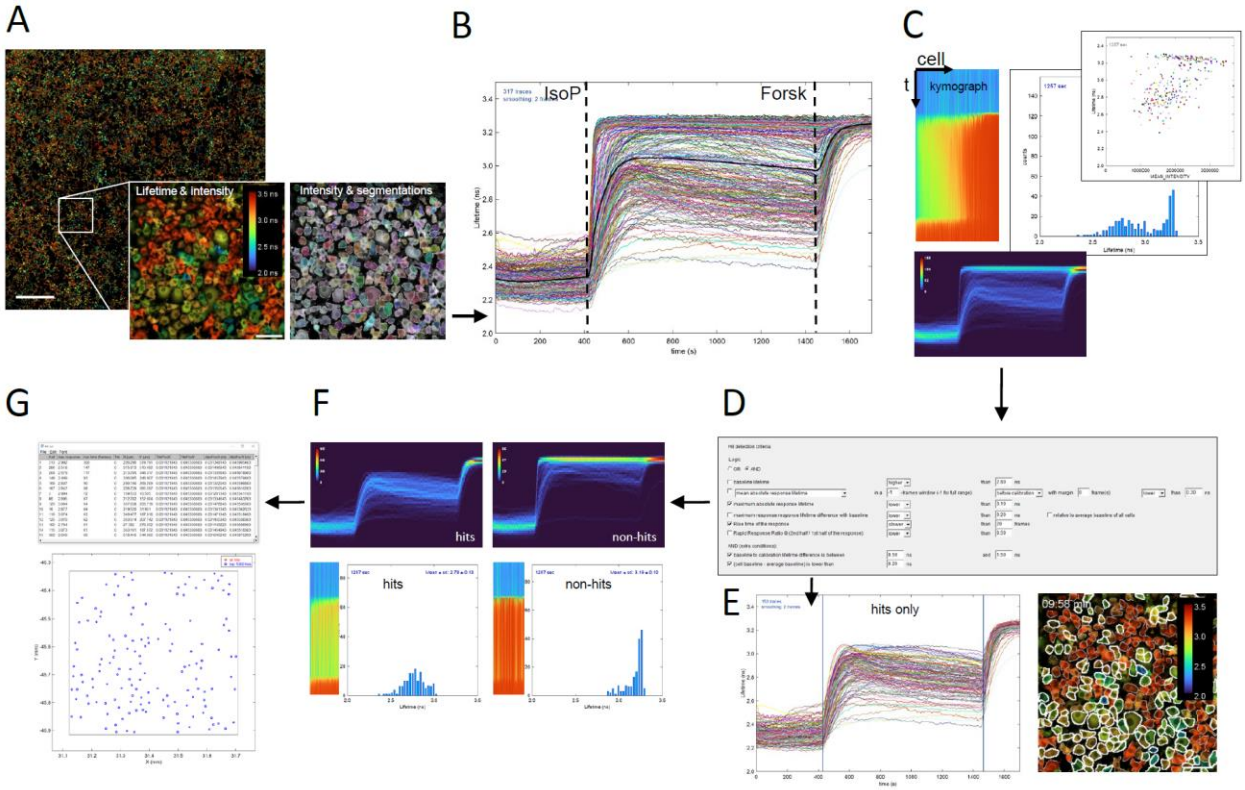

Fig. 4. Time-lapse FLIM analysis and hit detection Fiji macro. (A) *Stitched multi-tile intensity image overlay with the fluorescence lifetime image. The lifetime image can be either average photon arrival times ('Fast FLIM') or calculated average lifetimes from two lifetime components. Ratiometric images can also be used. Scale bar: 1000 µm.* ***Inset:*** *Left – Zoom-in of lifetime image of cells after stimulation with isoproterenol; Right – Zoom-in showing cell segmentation as outlines. Scale bar: 100 µm.* ***(B)*** *Lifetime time traces of all 298 segmented cells in a single tile of Cos7 cells (a mix of ADRB2 KO and WT cells). Cells are stimulated with 40 nM isoproterenol (IsoP), followed by a calibration with forskolin (Forsk). Stimulation and calibration time points may be automatically calculated from the average of all traces (thick black line) or entered manually.* ***(C)*** *The script generates several informative visualizations. Shown are a 'kymograph' representation of fluorescence lifetime vs time in all cells, sorted on response magnitude (top-left); a normalized data density graph (2D histogram of lifetime vs time, with cell counts in false color), convenient when analysing thousands of cells (bottom); and (optionally animated) histograms of the fluorescence lifetimes over time (middle) and scatterplots of lifetime vs secondary parameters like cell intensity, cell area or intensity of an additional fluorescence channel of choice (top-right).* ***(D)*** *Hit selection dialog showing various optional criteria. These can be used separately or combined, allowing to screen for a large variety of dynamic phenotypes.* ***(E)*** *Based on the criteria, hit cells are determined and visualized through a 'hits only' lifetime traces plot (left). Blue vertical lines indicate the chosen hit detection time window. The hit cells are outlined with white lines on the lifetime-intensity overlay image (right).* ***(F)*** *Additional visualizations of hit cells (left) and non-hit cells (right), in density graphs, response-sorted kymographs and time-lapse histograms.* ***(G)*** *Microscope stage coordinates of the hit cells are shown in tables, and a 2D graph. The script also generates a .rgn file with positions, which can be directly read by LAS X Navigator, for e.g. photoactivation, high-resolution imaging etc. For visualization of animated plots, see the web site (https://imagej.net/plugins/fast-hippos).*

A first test of the screening pipeline: correct identification of hits, low false positive rates

To assess the performance of the entire screening pipeline, we tested its accuracy to distinguish a small fraction of β-adrenergic signaling-deficient Cos7 cells from WT cells. For this experiment, we generated polyclonal populations of cells expressing iCas9 and either gRNAs against the β-adrenergic receptor (ADRB2 KO) or the G protein $G_{\alpha s}$ (GNAS KO) (Fig. 5A) as well as non-targeting (NT) control cells, using an empty pXPR_050 lentiviral vector. After selection for iCas9 with puromycin for two days and induction with doxycycline for four additional days, polyclonal KO populations were phenotypically characterized by stimulation with 40 nM isoproterenol (IsoP), followed by calibration of responses with 25 µM forskolin (FSK; Fig. 5B (i), (ii), (iii)). As expected, NT control cells exhibited a homogenous and sustained response to isoproterenol, which saturated the FRET response, while ADRB2 KO and GNAS KOs displayed decreased cAMP responses. However, these cells retained proper forskolin-induced activation, confirming intact adenylyl cyclase functionality.

To simulate rare hits encountered in large-scale screens, NT control cells were mixed with approximately 2% each of polyclonal ADRB2 KO and GNAS KO cells and responses to isoproterenol were recorded (Fig. 5C). Image data were processed with our Fiji pipeline, selecting hits with a maximum lifetime response lower than 3.1 ns that also have an intact calibration response (See Supplementary M&M). Out of the 14,000 imaged cells, 473 (~3.4%) were classified as hits and photoactivated with the 405 nm diode laser. Note that the ADRB2 and GNAS KO cell populations were polyclonal and thus heterogeneous, exhibiting some WT responses, which likely explains the discrepancy between 4% input KO cells and 3.4% of cells recovered.
Next, photoactivated cells were sorted for mCherry brightness by FACS into a single well (see Supplementary M&M), retrieving ~71% of the red cells. The cells were then expanded for 15 days, re-analysed by FLIM assays, and subjected to Sanger sequencing for gRNA identification. FLIM assays using isoproterenol as stimulation confirmed that ~90% of recovered cells exhibited the KO phenotype, indicating a false-positive rate in the FLIM assay, tagging and sorting steps combined of ~10% (Fig. 5D, 5E). Sanger sequence analysis further confirmed this observation, showing both ADRB2 and GNAS gRNA abundance and negligible NT contamination. In both the sequencing results and in the FLIM confirmation assay, a relative decrease in GNAS KO abundance is noticeable in the expanded population (Supplementary Material 3 and Fig. S2A, S2B). This is likely due to a growth disadvantage of GNAS KO cells (Ding *et al*, 2020; He *et al*, 2024) as compared to the ADRB2 KO and mis-sorted NT control cells during the expansion phase, and as a result, the false positive rate of ~10 % is probably an over-estimation. Notwithstanding, the observed false positive rate is within an acceptable range, validating the robustness of the screening pipeline.

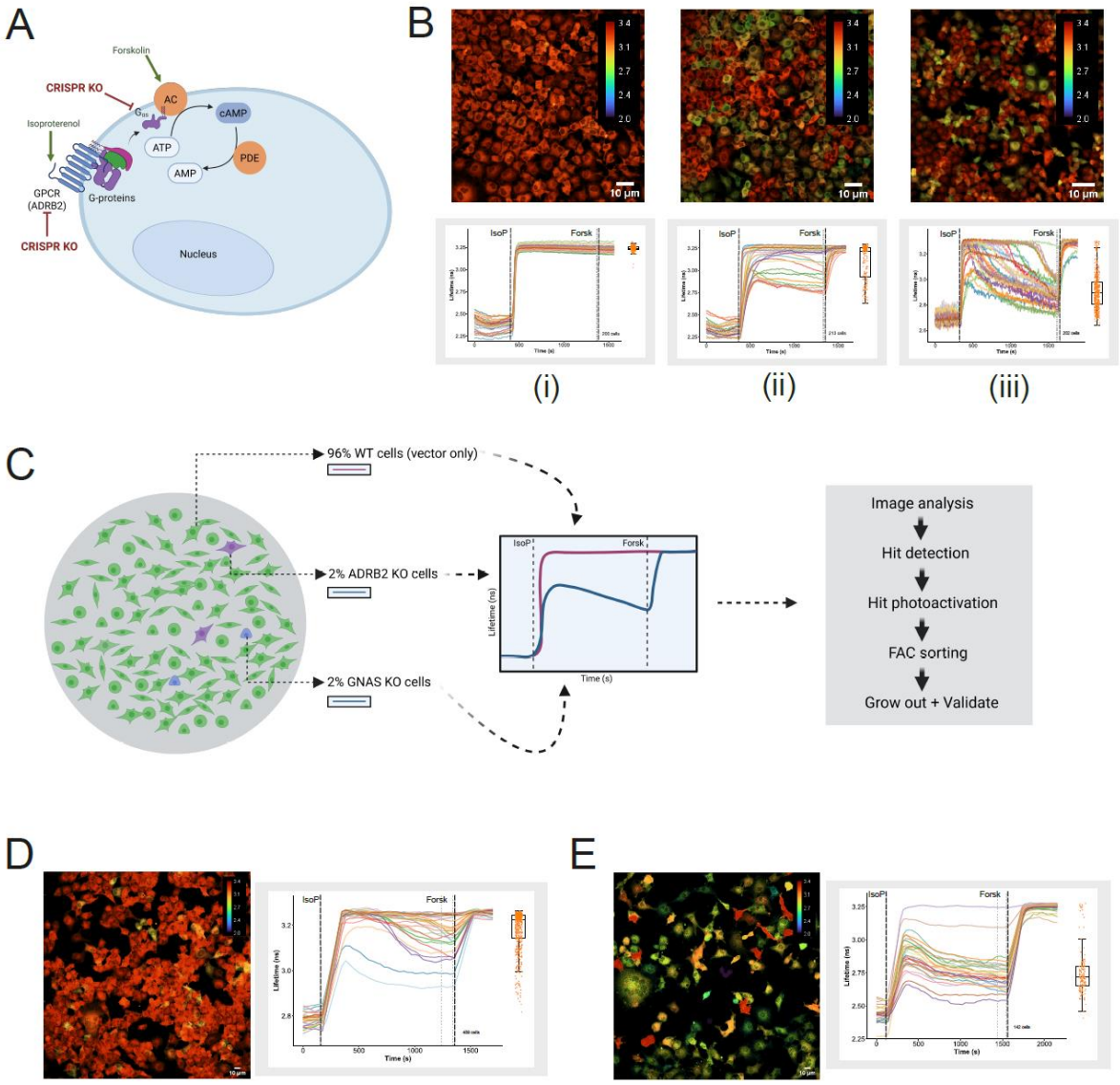

Fig. 5. First test of the screening pipeline: (A) *Schematic showing the cAMP signaling pathway.* ***(B)*** *Top – FLIM images of Cos7 Green monkey kidney cells, Bottom – Representative FLIM traces when stimulated with 40 nM isoproterenol and calibrated with 25 µM forskolin in* ***(i)*** *Cos7 H250 WT,* ***(ii)*** *Cos7 H250 ADRB2 polyclonal KO and* ***(iii)*** *Cos7 H250 GNAS polyclonal KO; n=4 for each.* ***(C)*** *Schematic representation of the experiment outline where ~96% Cos7 H250 WT cells are mixed with ~2% each of polyclonal ADRB2 and GNAS KOs. They are then screened and selected for low amplitude phenotypes.* ***(D)*** *Left - FLIM image of Cos7 cells before selecting for hits, Right - FLIM data of cells stimulated with isoproterenol and forskolin before hit selection.* ***(E)*** *Left - FLIM image of Cos7 cells after hit selection and expanding for 15 days and Right - corresponding FLIM data. For all time trace plots, twenty randomly selected traces are displayed along with the quantification of lifetime (at the time indicated with grey dotted line) of all cells in the boxplots. Nr of analysed cells are indicated at the bottom right in the graphs. Scale bar: 10 µm. IsoP: addition of 40 nM isoproterenol; Forsk: addition of 25 µM forskolin.*

Checking sensitivity and false positive rates: a Dolcetto Library benchmark experiment

Currently, the number of hits that can be photoactivated is limited to a few thousand per run, due to time constraints. The minute amounts of DNA recovered for next-generation sequencing pose high demands on the DNA recovery step to limit false-hit rejection, in particular for larger gRNA libraries and limited gRNA coverage. Therefore, we decided to further scrutinize DNA recovery and false-hit rate. Extensive optimization of gRNA recovery in low cell numbers showed that best results were obtained with a low-fidelity Taq polymerase (rather than with e.g. high-fidelity Phusion polymerases), using 35 PCR cycles and paying special attention to working with DNA-free and DNAse-free stocks (for more details, see M&M and Supplementary M&M).

To determine the sensitivity in gRNA detection with low numbers of cells, as well as the sensitivity and specificity of photo-activation and cell sorting, we made use of the Dolcetto gRNA library (Sanson *et al*, 2018). This library contains 57,050 gRNAs in Set A and 57,011 gRNAs in Set B and no gRNA is present in both libraries. Cos7 H250 cells were either transduced with lentiviruses encoding Dolcetto gRNA library set A or Dolcetto gRNA library set B at a multiplicity of infection (MOI) of approximately 0.3 and 0.4 respectively, ensuring that most of the transduced cells received only a single gRNA. As in this experiment the gRNA sequences merely functioned as DNA barcodes, it is in this case irrelevant that a human library is used in green monkey Cos7 cells. Following selection with puromycin, cells transduced with set A were photoactivated by exposure to light from a 405 nm LED, and then mixed with set B at 1:4 ratio (set A: set B). Different numbers of photoactivated cells were isolated by FACS (200, 500, 2000, 5000, and 10,000 per sample, in triplicate), and gRNAs were amplified by PCR and sequenced as described in the M&M (Fig. 6A). As expected, most of the sequence reads (98.2 – 100%) are unique gRNA sequences (97.4 – 100%) and mapped to gRNAs of set A, indicating that the false-positive rate was below 2.6%, worst case, and < 1% on average (Fig. 6B). Normalized count distributions are also shown (Fig. 6C). Our data also show that the sensitivity of gRNA detection slightly decreased in samples that contained a higher number of cells (Fig. S3A).

In summary, this experiment shows that our pooled, optical CRISPR screening platform has high specificity with regard to recovery of gRNA sequences contained in the tagged cells and that the sensitivity of detecting DNA in photoactivated cells was high enough to accommodate the expected small samples.

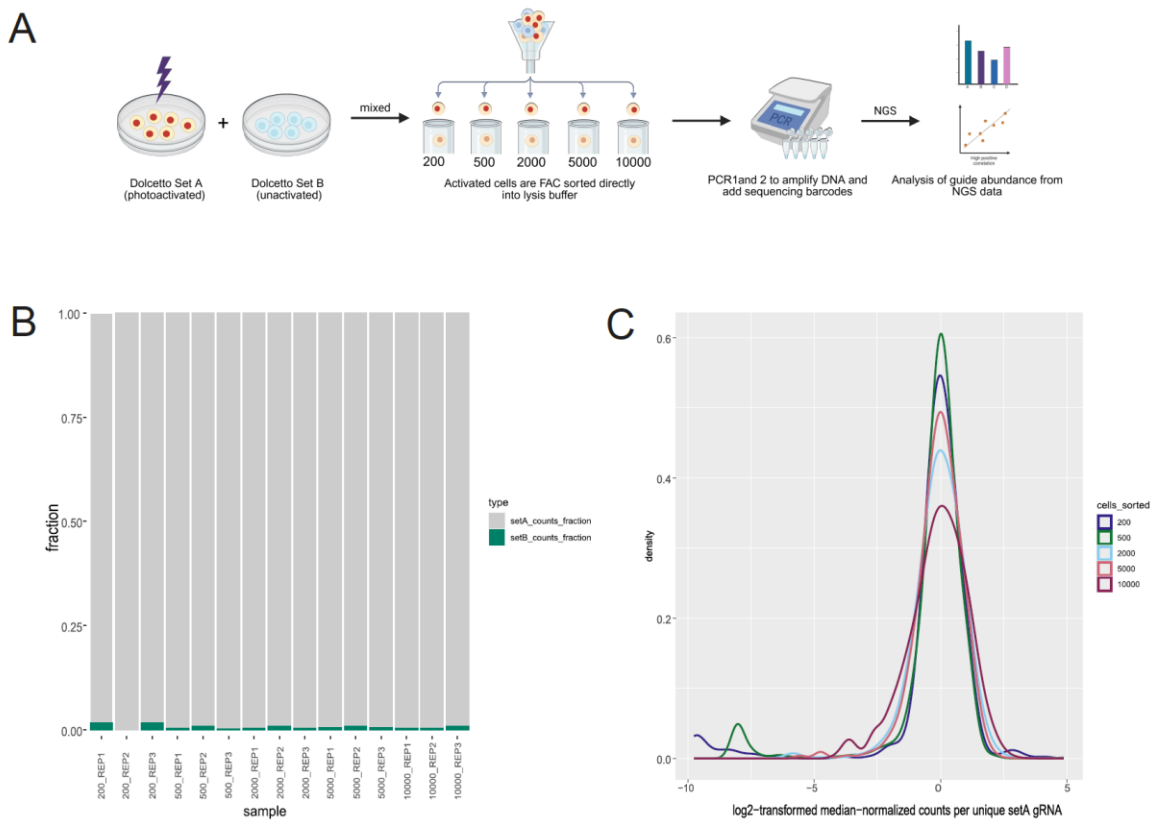

Fig. 6. Dolcetto library benchmark experiment: (A) *Schematic illustrating the experiment. Photoactivated Dolcetto SetA cells are mixed with non-activated Dolcetto SetB cells, followed by FAC sorting different numbers (200, 500, 2000, 5000, 10000) of the photoactivated cells. This is followed by cell lysing, readout amplification via PCR and subsequent next-generation sequencing (NGS) and analysis.* ***(B)*** *Fraction of reads mapped to gRNAs of SetA and SetB after cell sorting and sequencing.* ***(C)*** *Normalized count distributions for each unique gRNA of SetA after cell sorting and sequencing. Experiment were done in triplicate.*

Design of a screening library for cAMP response dynamics

Next, we set out to perform an actual screen with a custom gRNA library of moderate size, which includes most of the genes that might conceivably be involved in shaping the dynamics of receptor-mediated cAMP signals. The library includes genes that may affect the magnitude of the response, such as G-Protein coupled receptors, $G_{\alpha s}$, adenylate cyclases and phosphodiesterases (~40 genes). It also included genes that may alter the longevity of the cAMP signals, for example, genes known or suspected to be involved in receptor internalization, such as receptor kinases, arrestins, clathrin, dynamins, the AP2 complex and vesicle-trafficking genes (~20 genes). Additionally, we included a number of cAMP effector genes, which might function in regulatory feedback loops, as well as genes that might affect the unstimulated baseline of cAMP concentration, and a number of controls. Finally, several more distantly related genes were included to increase the potential for discovering new members involved in the pathway. A total of 318 genes were included (See Supplementary File S1, File S2). More details of how these genes were curated are in Supplementary Material 4.

Screening in HeLa H250 cells requires additional optimization of the phototagging paradigm: PA-Janelia-Fluor646.

During initial screening tests with HeLa H250 cells, we noted that cell-to-cell expression levels of the FLIM sensor as well as PA-mCherry became variable, up to 20-fold, after short time subculturing (Fig. 7A). While this variability poses little issue for FLIM readout of cAMP levels because fluorescence lifetime is concentration-independent, it presents a significant challenge for cell tagging. Even minimal accidental photoactivation of a bright bystander cell (e.g., when the nuclei of a hit cell and a wild-type bystander are in close apposition) can render the bystander as bright as a fully photoactivated hit cell with 20-fold lower expression, thereby compromising the specificity of downstream cell sorting. We thus set out to develop an alternative, more stable phototagging method using a photoactivatable chemical fluorophore.

HeLa H250 cells were loaded with the photoactivatable chemical fluorophore PA-Janelia-Fluor646. This cell-permeable dye covalently binds primary amines present throughout the cells via an N-hydroxysuccinimide (NHS) group, offering the advantage of cloning-free application across all cell lines (Fig. 7B). To evaluate its compatibility with the live-cell screening pipeline, we showed that PA-Janelia-Fluor646 tagging is non-toxic, it does not affect baseline- or agonist-induced cAMP levels, and gives negligible crosstalk with the Epac FRET sensor (Supplementary Material 1; Fig. S1). As the reactivity of NHS is significantly higher at basic pH values, loading of cells with PA-Janelia-Fluor646 could be boosted by briefly pre-incubating the cells with ammonium chloride (Fig. 7C). Upon photoactivation with a 355 nm UV laser, PA-Janelia-Fluor646 signals appeared over 5-fold brighter than fully activated PA-mCherry signals in FACS experiments (Fig. S1 F). In summary, PA-Janelia-Fluor646-tagging presents a novel and cloning-free tagging strategy for pooled screening experiments.

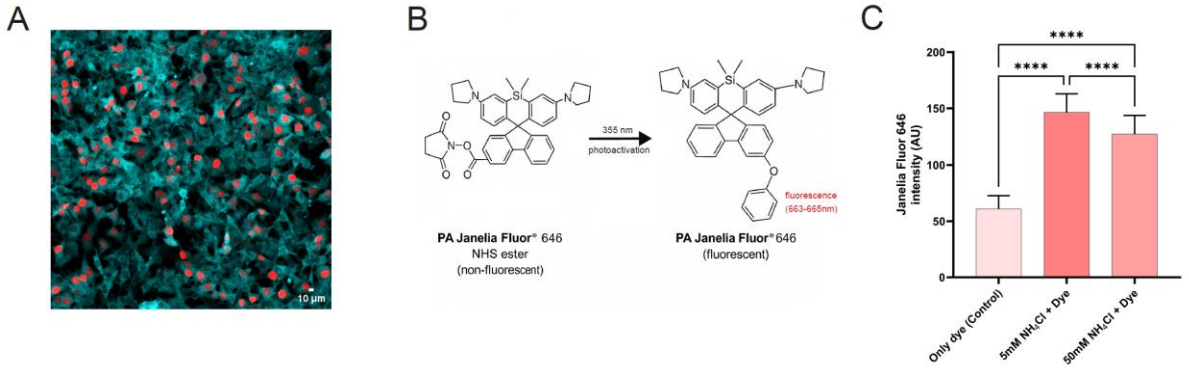

Fig. 7. Photoactivation using PA-mCherry and the PA-Janelia-Fluor646: (A) *HeLa H250 cells expressing the reporter construct with selected nuclei photoactivated using a 405 nm laser. mTurquoise intensity is depicted in cyan. PA-mCherry intensity is depicted in red, showing high variability.* ***(B)*** *Chemical structure of non-activated and activated PA-Janelia-Fluor646 dye.* ***(C)*** *Boosting dye intake in HeLa H250 WT cells by pre-incubating them in various concentrations of ammonium chloride. Cells were pre-incubated with ammonium chloride for 2 minutes. ****: p<0.0001; One-way ANOVA with multiple comparisons test. Scale bar: 10 µm.*

Proof-of-concept screen 1: low cAMP responder screen

We first characterized the isoproterenol response dynamics in control cells to establish statistics for the HeLa H250 WT cells (Fig. 8A). Like in Cos7 H250 cells, addition of isoproterenol triggered a rapid increase in cAMP after 10 ± 5 s. cAMP then remained high for an average of 15 ± 5 min before slowly returning to baseline. A large pool of cells was imaged to establish the frequency of outliers, which will affect the fraction of false hits and missed hits. The time-course of this response also dictates what sampling speed is needed to capture the dynamics, which in turn determines how many cells/fields of view can be included in the screen, given the optimized imaging speed as determined in Supplemental Material 2.

As a first proof-of-principle screen we used our cAMP response dynamics library and aimed to identify genes that upon KO attenuate the cAMP increase in response to the β-receptor agonist isoproterenol. Expected hits would be genes that in WT cells positively contribute to either the magnitude or the longevity of cAMP formation, or genes that strongly downregulate cAMP clearing. Thus, KO of these genes should result in low amplitude isoproterenol responses or in short-duration transient responses. A 6-minute interval suffices to capture the relatively slow sustained phase of the response and allows a total of 240 imaging tiles to be acquired. An one-hour experiment thus contains 10 frames: baseline (frames 1-2), response (frames 3-8) and calibration (frames 9-10).

For the analysis the following criteria were used: (i) Cells should occupy a minimum of 220 pixels, causing CellPose to segment on average of 30,000 cells per sample; (ii) The calibration response (lifetime after forskolin addition minus the baseline value) was required to be at least 0.3 ns in order to reject dead cells and debris; (iii) Cells with baseline lifetimes differing more than 0.3 ns from the population average were rejected; and (iv) Upon stimulation with isoproterenol, cells were called low-responder hits when the average lifetime in frames 6, 7, and 8 was within 0.4 ns from the baseline lifetime (average of frame 1 and 2), i.e. those cells that showed > 50% reduction in response as compared to the average population in NT control cells (Fig. 8B (i), (ii)). With these criteria, we found a false-positive rate of 2.2% in control cell samples, while significantly higher hit rates were detected in the KO samples across three replicates: 5.3%, 4.9%, and 6.2%, respectively (Fig. 8C). Cells were phototagged, sorted and sequenced. The primary hit selection was based on a statistical analysis with DESeq2 and MAGeCK's Robust Rank Algorithm. Three genes stood out, namely the Adrenergic Beta Receptor 2 (ADRB2), G protein $G_{\alpha s}$ (GNAS), and Adenylate Cyclase 6 (ADCY6) **-** all key regulators of cAMP signaling (Fig. 8D), which together form the main axis in classical cAMP signaling. In addition, further hits were genes that had at least 1 gRNA enriched in all 3 replicates: Phospholipase C Delta 4 (PLCD4), A-kinase anchoring protein 11 (AKAP11), Sodium-hydrogen antiporter 3 regulator 1 (SLC9A3R1), Vacuolar protein sorting-associated protein 26A (VPS26A) and Sortin Nexin 13 (SNX13) (Fig. 8E).

Validation of hits in the low-responder screen

To follow up on these findings and validate the three main hits, monoclonal KO cell lines for candidate hits were made, confirmed by Sanger sequencing and microscopically tested using the same assay as the screen. As shown in Fig. 8F (ii)-(iv), ADRB2 and ADCY6 KO lines exhibited strongly diminished cAMP responses, whereas the response in GNAS KO cells was abolished completely.

HeLa cells express at least 5 different adenylyl cyclase isozymes, namely: ADCY3, ADCY6, ADCY7, ADCY9 and ADCY10 (Simko *et al*, 2017; Bernatchez *et al*, 2003) with partial functional overlap. Our findings suggest that ADCY6 is the primary adenylyl cyclase coupling to $G_{\alpha s}$ in HeLa cells (Fig. 8F (ii)). The partial

response in ADRB2 KO cells (Fig. 8F (iii)) was perhaps to be expected: isoproterenol is an agonist to both adrenergic receptors, ADRB2 and ADRB1, and thus the remaining response might be mediated by low-level ADRB1 expression, although the human protein atlas reports negligible expression in HeLa cells (Pontén *et al*, 2008). Similarly, the near-complete wipeout of the response in GNAS KO cells (Fig. 8F (iv)) is no surprise because GNAS encodes for the only isoform of $G_{\alpha s}$.

We also sought to validate the additional hits identified in the screen (Fig. 8E) by generating their polyclonal CRISPR KO cell lines. Out of the five weaker hits identified (PLCD4, AKAP11, SLC9A3R1, VPS26A, SNX13), two genes (VPS26A, SNX13) consistently validated in FLIM experiments (Fig. 8G). Shown is the enrichment (fold over WT control) of cells abiding to the screening criteria in polyclonal KO cell lines (Fig. 8G, 8H). Interestingly, both VPS26A and SNX13 have regulatory roles in endosomal sorting and recycling (Henne *et al*, 2015; Shi *et al*, 2006; Li *et al*, 2014a; Zheng *et al*, 2006; Seaman, 2012). While their exact role in diminishing the response to isoproterenol is outside the scope of this paper and remains to be determined, they present a strong phenotype since they were detected in all repeats of the validation tests. In conclusion, these validation studies confirm the sensitivity and reliability of the screening pipeline in identifying key cAMP regulators.

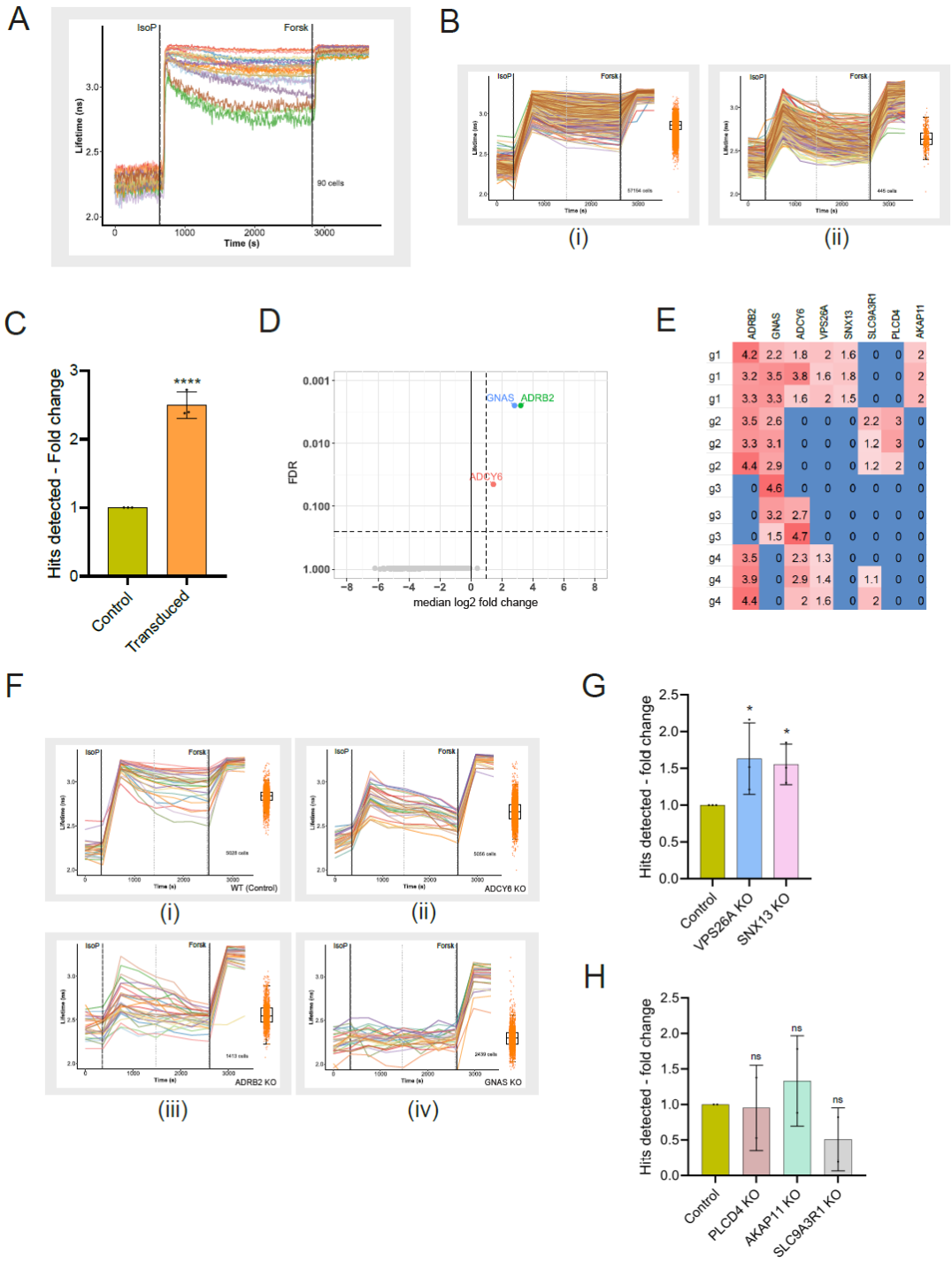

Fig. 8. Detecting and validating hits in the low responder screen: (A) *Responses of cells expressing the Epac-based cAMP sensor in HeLa cells (HeLa H250 WT) stimulated with 1 µM isoproterenol and 25 µM forskolin, imaged with high time resolution. Time-trace plots visualized as detailed in Fig. 5.* ***(B) (i)*** *Responses of hundreds of cells screened in Willco well 1 of Replicate 1 to isoproterenol and forskolin at Frame 2 and Frame 8, respectively.* ***(ii)*** *Hit cells identified in this well using screening parameters as detailed in the text.* ***(C)*** *Relative frequency of hits across 3 replicates of transduced samples, as compared*

to the control HeLa H250 WT cells from the screens. Statistical analysis was with an unpaired, one-tailed t-test. ***(D)*** *Primary hits - genes where targeting gRNAs were significantly (FDR ≤ 0.25) and substantially (median log2 fold change ≥ 1) enriched in the sorted population for low responders.* ***(E)*** *Heat map displaying the enrichment (Log2Foldchange values) of gRNAs of primary and secondary hits across all 3 replicates.* ***(F)*** *Representative traces from validation experiments showing* ***(i)*** *HeLa H250 WT (n=4),* ***(ii)*** *HeLa H250 ADCY6 KO (n=4),* ***(iii)*** *HeLa H250 ADRB2 KO (n=3) and* ***(iv)*** *HeLa H250 GNAS KO (n=3). Time-trace plots visualized as detailed in Fig. 5. KO differ statistically significant as determined using one-way ANOVA - ***** ***(G)*** *Relative frequency of hits in VPS26A and SNX13 polyclonal KO populations; n=3 for each. Control denotes HeLa H250 WT cells. Statistical analysis: unpaired, one-tailed t-test; VPS26A KO: p=0.0435; SNX13 KO: p=0.0126.* ***(H)*** *Relative frequency of hits as compared to the control HeLa H250 WT cells from the screen PLCD4, AKAP11 and SLC9A3R1 polyclonal KO populations; n=2 for each. PLCD4 KO: p=0.4604 (ns); AKAP11 KO: p=0.2688 (ns); SLC9A3R1 KO: p=0.1290 (ns). For all panels: ns not significant; * p < 0.05; ** p < 0.005; **** p < 0.0001; n = number of experiments performed; IsoP denotes addition of 1 µM isoproterenol; Forsk denotes addition of 25 µM forskolin. Note that the control data used for statistical testing in (G) and (H) are those taken during the screen.*

Proof-of-concept screen 2: high cAMP baseline screen

In a second proof-of-principle screen we used our screening pipeline and the cAMP gRNA library to test for genes that affect the basal cAMP concentration in these cells, i.e. in unstimulated cells. A priori, we may expect to recover genes that are either involved in cAMP breakdown, that affect tonic (agonist-independent) receptor signaling, negative regulators of $G_{\alpha s}$ signaling and genes that positively affect $G_{\alpha i}$ and those that are involved in receptor internalization.
The selection criteria were chosen to identify cells that, upon gene KO, experienced increased basal levels of cAMP. We prepared pooled KO cells as before and collected a total of 304 imaging tiles, two time points each, which required a total of 12 minutes. After that, cells were stimulated with forskolin in one control well for each replicate, solely to check for cell health and magnitude of the FRET span. In this screen no forskolin calibration criterion was included because it would lead to rejection of cells with very high baseline.

Automated analysis identified an average of 40,000 cells per sample, and hits were defined as cells displaying a baseline lifetime differing from the population average (2.27 ns) by over 4 times the SD (0.077), i.e. with lifetime > 2.6 ns (Fig. 9A). Cells fulfilling this single criterion (τ_b > 2.6 ns) were photoactivated, isolated by FACS and subjected to NGS analysis. The primary hit selection was based on a statistical analysis with DESeq2 and MAGeCK's Robust Rank Algorithm. Rap guanine nucleotide exchange factor 3 (RAPGEF3), also known as Epac1 (Fig. 9B) was identified as the primary hit. Further hits were genes that had at least 1 gRNA enriched in all 3 replicates: the Somatostatin Receptor 1 (SSTR1), Phosphodiesterase 1C (PDE1C), Adaptor Related Protein Complex 1 Subunit Gamma 2 (AP1G2) and Adaptor-related protein complex 2, alpha 1 (AP2A1) and genes which had at least 2 gRNAs enriched in 2 replicates with a Log2Foldchange value of higher than 1: Regulator of G Protein Signaling 14 (RGS14) (Fig. 9C).

Validation of hits in the baseline screen

For validation, polyclonal KO cell lines of the hit genes were generated, confirmed by Sanger sequencing and tested in FLIM experiments as well as by a cAMP ELISA assay (see Supplementary M&M). The FLIM analysis of RAPGEF3 KO cells indeed showed very high baseline values; additionally, these cells were

unresponsive to stimulation with 25 µM forskolin and showed aberrant fluorescence distribution (Fig. 9D (ii)). Based on the latter, this hit most likely is an artifact of the screen. Indeed, RAPGEF3/Epac1 is the cAMP sensing moiety of our FRET-FLIM sensor, and iCas9 editing would thus delete most of the Epac1 sequence, as well as the fluorescence acceptor moiety of the FRET probe (Fig. S4). This leaves cells with only an mTurquoise2 FRET donor attached to part of the Epac protein, which causes erroneous cellular localization and, in absence of FRET, obviously displays a high fluorescence lifetime. In line with this notion, the ELISA analysis indicated normal baseline cAMP levels in these cells (Fig. 9E). Be that as it may, the observation served as a good positive control that we readily pick out long lifetimes, even in the absence of additional viability controls.

Of the remaining hits, SSTR1, RGS14, and PDE1C showed significantly elevated baseline lifetimes in FLIM analysis (Fig. 9F) whereas AP2A1 and AP1G2 did not, when retested in polyclonal KO cells. SSTR1 may be expected to affect cAMP basal levels because the receptor is coupled to $G_{\alpha i}$ and reportedly displays constitutive activity (Ben-Shlomo *et al*, 2010). Its KO would release the $G_{\alpha i}$ brake from adenylate cyclases and thereby increase cAMP levels.

RGS14 is a GTPase-activating protein (GAP) that, among other things, accelerates GTPase activity of $G_{ao/i}$ subunits, thereby turning them off early, which also releases the brake on adenylate cyclases (Wang *et al*, 2024). Lastly, KO of the phosphodiesterase PDE1C – and thus member of the only protein family known to catalyze breakdown of cAMP **-** is also likely to affect cAMP breakdown**,** and thus increase cAMP levels, in a cell line with basal $G_{\alpha s}$ / AC activity (Azevedo *et al*, 2014; Pratt *et al*, 2019; Zhang *et al*, 2012).
Note that the ELISA measurements were less sensitive in picking up increased basal cAMP levels than our FLIM assay (Fig. 9E, 9F), showing marginal increase in polyclonal SSTR1, while RGS14 KO, PDE1C KO, AP2A1 KO and AP1G2 KO were comparable to WT ($p = 0.03$ (*), $p= 0.2$ (ns), $p=0.2$ (ns), $p=0.3$ (ns) and $p= 0.08$ (ns) respectively). This discrepancy likely reflects the difference between single-cell and bulk measurements. ELISA assays capture population cAMP levels, averaging the responses of KO and WT-like cells in these polyclonal populations. In contrast, our FLIM data reflect single-cell cAMP levels, and the analysis focuses on the percentage of cells that comply to the hit criterion, i.e. those cells that display the strongest phenotype. This allows detection of KO-specific phenotypes within heterogeneous populations much more sensitively.

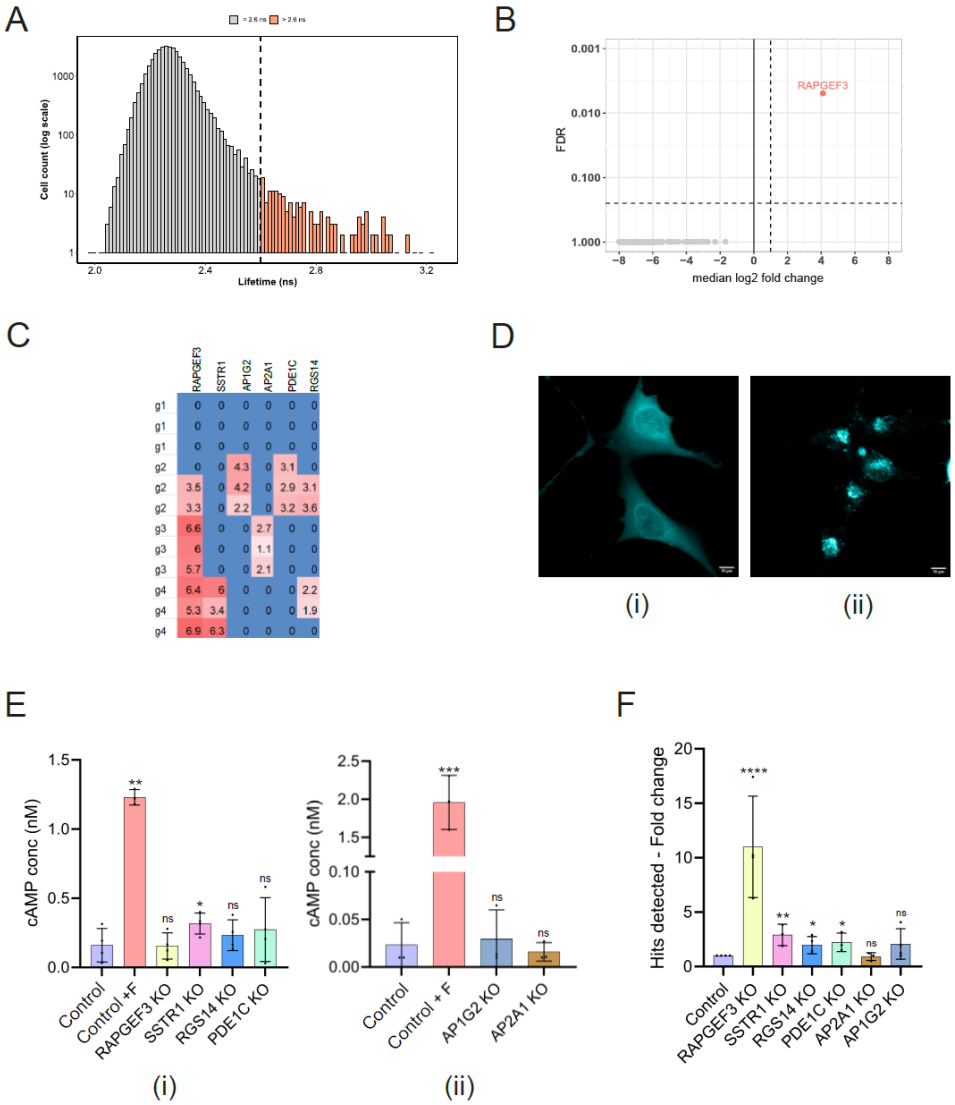

Fig. 9. Detecting and validating hits in the baseline screen: (A) *Histogram depicting the distribution of baseline lifetimes of HeLa H250 cells transduced with the cAMP library (Willco well 1 of replicate 1). The threshold for detecting hits was set at 2.6 ns (highlighted in orange).* ***(B)*** *Primary hit - gene where the targeting gRNAs were significantly (FDR ≤ 0.25) and substantially (median log2 fold change ≥ 1) enriched in the sorted population for increased baseline cAMP compared to the reference population.* ***(C)*** *Heat map displaying the enrichment (Log2Foldchange values) of gRNAs of primary and secondary hits across all 3 replicates.* ***(D) (i)*** *HeLa H250 WT control cells expressing the Epac sensor and* ***(ii)*** *RAPGEF3 KO cells with erroneous sensor localization. mTurquoise intensity is depicted in cyan.* ***(E)*** *ELISA analysis of basal cAMP concentrations in different HeLa H250 polyclonal KO cell lines; n=3. Statistical significance of difference with control WT cells:* ***(i)*** *Control + Forskolin: p=0.0050; RAPGEF3 KO: p=0.4711; SSTR1 KO: p=0.0356; RGS14 KO: p=0.2060; PDE1C KO: p=0.2095;* ***(ii)*** *Control + Forskolin: p=0.0003; AP1G2 KO: p=0.4008; AP2A1 KO: p=0.3180.* ***(F)*** *Relative frequency of hits for the indicated HeLa H250 polyclonal KO cell lines; n >=2. RAPGEF3 KO: p<0.0001; SSTR1 KO: p=0.0055; RGS14 KO: p=0.0381; PDE1C KO: p=0.0103; AP2A1 KO: p=0.3485; AP1G2 KO: p=0.0872. For all panels, statistical analysis was performed using an unpaired, one-tailed t-test. ns, not significant; * p < 0.05; ** p < 0.005; *** p < 0.0001; n = number of experiments performed.*

DISCUSSION

In this study, we combine high-speed FRET-FLIM imaging, automated analysis, and a streamlined CRISPR screening and processing pipeline, to extend imaging-based pooled screening to dynamic phenotypes. We were able to record FLIM time-lapses in ~130,000 cells per replicate, allowing 100× coverage of a 318-gene, 1272-gRNA library with necessary controls across three replicates within just three days. As the relevance of dynamic signaling at the single-cell level has been previously established, this platform now allows identification of genetic regulators that influence specific temporal features of a signaling response. By moving beyond endpoint or static phenotypes such as cell viability or protein expression (Reicher *et al*, 2024; Yan *et al*, 2021) our approach expands the capabilities of pooled CRISPR screening into the dynamic domain.
To achieve this, several steps in the screening workflow were systematically optimized (discussed more extensively in Supplementary M&M and Supplementary Discussion). Stable cell lines were generated and characterized, imaging conditions were refined to balance acquisition speed and spatial resolution, and a Fiji analysis macro was generated to quantify key kinetic parameters and identify hits. Hit tagging, FACS-based recovery, and DNA extraction from low cell numbers also required substantial optimization, with emphasis on minimizing false positives while maintaining sufficient sensitivity to detect phenotypic changes. We tested feasibility of dynamic pooled screening using mixed populations of Cos7 H250 cells, and introduce a new specificity benchmark using the Dolcetto libraries. We also show performance of the pipeline in two proof-of-principle screens that target distinct kinetic features of cAMP signaling and identify hits with high reproducibility.

Our study is primarily focused at establishing the necessary pipeline and should also prove valuable as a starting point for setting up pooled dynamic screens beyond the use of FRET-FLIM screening and cAMP signaling. For example, our analysis script also supports simple intensity and ratio image data, and it can be readily tweaked to accommodate a variety of other dynamic screens, such as the temporal translocation of fluorescently tagged proteins in cells (Kanfer *et al*, 2021), protein degradation studies, as well as morphometrical data (Hasle *et al*, 2020) on e.g. cell migration, lamellipod mobility, neurite outgrowth and more. Indeed, the software can be adapted to any quantitative dynamic phenotype discernable by microscopy.

This study does not aim to provide an exhaustive analysis of genes involved in shaping cAMP dynamics. Given the design of the gRNA library, which targets components of the cAMP pathway and only a limited number of genes with no known involvement in cAMP signaling, we could expect to recover mainly known pathway components. In addition, subtle phenotypes in cAMP signaling, including localized nanodomains or hotspots of cAMP turnover, cannot be detected with our cytosolic FRET-FLIM sensors. Another limitation is that strong agonists such as isoproterenol cause a massive accumulation of cAMP, which saturates the FRET sensor and may mask certain aspects of cAMP dynamics, particularly in Cos7 H250 cells. This could be improved with FRET-FLIM sensors with a range of affinities that have been reported (Zanetti *et al*, 2025; Massengill *et al*, 2021).

In the proof-of-concept screen for low responders, we identify the main members of the cAMP stimulatory cascade: the receptor ADRB2, G protein GNAS and one specific isoform of adenylate cyclase, ADCY6. While gRNAs against other ACs were present in the library, these did not come up in the screen, suggesting that ADCY6 is dominant in cAMP production in HeLa cells, at least in the cytosol. In addition, VPS26A and SNX13 validated as secondary hits. Interestingly, both these genes are involved in aspects of membrane trafficking. VPS26A is part of the retromer complex and involved in recycling receptors to the plasma membrane (Seaman, 2012; Shi *et al*, 2006) while sorting nexin SNX13 is involved in endosomal

targeting of proteins (Zheng *et al*, 2006; Li *et al*, 2014a; Henne *et al*, 2015). Further studies are required to unravel how their KO attenuates cAMP signaling. In the proof-of-concept screen for regulators of baseline cAMP levels, the top hit is RAPGEF3, but this must be considered an artifact of our screening system since this is the gene on which our FRET sensor is based. The CRISPR edit is expected to take out most of Epac as well as the FRET acceptor (Fig. S4), leaving the cells with a long-lifetime donor, in a way providing a positive control for the detection scheme. Additional hits such as SSTR1, RGS14, and PDE1C - also known regulators of basal cAMP levels - were recovered (Pratt *et al*, 2019; Ben-Shlomo *et al*, 2010; Azevedo *et al*, 2014). Again, it is interesting that we found PDE1C and not the other members of the large PDE family present in our library. This indicates that PDE1C has global activity across the cytosol and at baseline concentrations of cAMP. In contrast, PDE8B is also expressed highly in HeLa cells but it has a restricted distribution in the cell which likely limits its effect on the cytosolic cAMP levels (Pontén *et al*, 2008). As these results validated repeatedly, they highlight the reliability and specificity of our screening pipeline.

We aim to follow up on this study by expanding to larger and unbiased gRNA libraries such as the human kinome (~760 genes) (Doench *et al*, 2016), the druggable genome (~2000 genes), and eventually gRNA libraries that cover the entire genome. The latter would involve extended imaging of ~10 million cells for 100× coverage. Technically, this can be achieved with our technology. For a one-hour time-lapse to capture all signaling dynamics, a genome-wide library could be screened within 2-3 weeks, using ~80 wells. By comparison, equivalent arrayed screens would require ~23,000 wells and over two years of continued imaging. Nevertheless, the throughput of our pipeline could be improved by focusing on the FLIM microscopy step, analysis and hit-calling, and the UV photoactivation step. Photoactivation may be sped up by activating hit cells in parallel, rather than sequentially, using e.g. a micro mirror device (Yan *et al*, 2021). The signal analysis script already runs on graphic processor cards and may be further sped up through parallel processing on better hardware as well. However, to our knowledge currently there is no hardware to speed up FLIM detection much beyond the speed provided by the Leica Falcon system (Alvarez *et al*, 2019) while retaining the accuracy and immunity to instrumental drift provided by TCSPC.

Finally, it is worth to spend some words on the chemical photo tagging method with PA-Janelia-Fluor646 for screening that we introduce. Previous studies have applied photoactivatable fluorescent proteins like PA-mCherry and Dendra2 (Yan *et al*, 2021; Kanfer *et al*, 2021) for this purpose. In our hands, expression levels of PA-mCherry were too variable in HeLa H250 cells to function as a reliable phototag. Therefore, loading and photoactivation of PA-Janelia-Fluor646 were optimized to provide a more reliable and brighter alternative. PA-Janelia-Fluor646 tagging requires no cloning and thus is also applicable to cells that are difficult to clone (such as iPSCs). On the other hand, PA-Janelia-Fluor646 is only weakly activated with 405 nm lasers, it requires shielding cells from bright ambient light, and its intensity fades faster than PA-mCherry, by almost 50% in just three hours (Fig. S1H). This necessitates that FACS processing is initiated within hours of the screen.

Together, this study takes a significant step toward integrating two powerful approaches—pooled genetic screening and dynamic single-cell imaging. High-speed imaging of single cell dynamics provides insight into cellular behavior and biological variability over time. To uncover regulators that shape these dynamics, pooled screens offer a scalable and unbiased solution. Combined, DynaScreen creates a generalizable platform to screen any imaginable phenotype, as well as to do systems biology, within realistic experimental timeframes.

MATERIALS AND METHODS

Making a stable cell line expressing iCas9 and Epac-S^{250} biosensor

HeLa (human cervical cancer cell line; CCL-2) and Cos7 (Green monkey kidney cells; CRL-1651) cells were cultured in DMEM supplemented with 10% fetal calf serum (FCS) and GlutaMAX (Gibco, Thermofisher #61965059). To generate stable iCas9-expressing lines, cells were transduced with the Edit-R iCas9 lentiviral vector (Dharmacon) and selected with 10 µg/mL blasticidin (Invivogen) for three days to enrich for transduced populations. Then, the HeLa iCas9 and Cos7 iCas9 cell lines were transfected with the Epac-S^{H250} , which contains the Epac-S^{H189} FRET sensor and HNS-PA-mCherry, connected with a self-cleaving 2A sequence (Fan & Steitz, 1998; Donnelly *et al*, 2001). This construct was transfected using the Tol2 transposon system (Klarenbeek *et al*, 2015; Kawakami, 2007). For more detailed information regarding testing and making these cell lines, see the Supplementary M&M.

gRNA/Library designing, cloning and transduction

Individual gRNAs and the cAMP library were cloned into the pXPR_050 lentiviral gRNA expression backbone (Addgene #96925). To produce lentivirus encoding the gRNA library or individual gRNAs, 10^6 Hek293 (Human kidney cells; CRL-1573) cells were used for transduction in the target cell lines. Detailed information regarding these steps is in the Supplementary M&M.

DynaScreen (Low responders and Baseline screens) – Preparing the cells

For both screens, cells were similarly prepared. The screens were conducted in three biological replicates. For the low responder screen each replicate was performed on different days using the same cell line and identical protocols. For the baseline screen, all replicates were performed on the same day. Steps are outlined here for *one* replicate.

On day 1, HeLa H250 iCas9 cells were seeded into five (seven for the Baseline screen) 10 cm dishes, each containing 500,000 cells. Cells were seeded as follows:

Plate 1 = Sample REP1 (Transduced + Puromycin)
Plate 2 = Control (Transduced – Puromycin)
Plate 3 = Control (Untransduced + Puromycin)
Plate 4 = Imaging Control (Untransduced – Puromycin)
Plate 5 = For counting cells next day
Plate 6 and 7 = Sample REP2, Sample REP3 (Transduced + Puromycin) [only for baseline screen]

On day 2, the plate designated for cell counting was used to estimate cell numbers, and the other plates were transduced with 128 µL of lentivirus (MOI = 0.3) carrying the library. Details of lentiviral library production and titer calculation are outlined in Supplementary M&M. On day 3, cells were passaged at 20% confluency, reseeded into new plates, and subjected to 2 µg/mL of puromycin selection while editing was induced by adding 2 µg/mL of doxycycline. Doxycycline was also added to the Imaging control, to keep the same culture conditions. On day 6, puromycin selection was discontinued, but doxycycline was maintained. Only the imaging control was split at 30% confluency, while transduced plates were allowed to proliferate.

The day before the screen (Day 8), 10 Willco wells (glass bottom, 35 x 10 mm; #HBSB-3522) were seeded with 150,000 cells each from the transduced sample, and 2 Willco wells were seeded with 150,000 cells each from the imaging control. Additionally, 2 wells were seeded with 10^6 cells each from the transduced sample to serve as t_0 reference controls. Penicillin-streptomycin (Invivogen) was added to all samples and controls to prevent contamination. On the day of the screen (Day 9), cells were visually inspected for health and confluence before proceeding.

DynaScreen (Low responders and Baseline screen) – Imaging the cells

Prior to imaging, cells are incubated with 5 mM NH_4Cl for 1 min, followed by replacement with FluoroBrite medium (FB medium) (Gibco, Thermofisher) containing 1 µM PA-Janelia-Fluor646 dye (Tocris Bioscience, #6150). Cells are incubated for 30 min at 37°C and then washed once with PBS and once with FB medium. Wells were subsequently filled with 2 mL FB medium and transferred to the microscope stage for imaging. FLIM experiments were conducted on a Leica Stellaris 8 FALCON confocal microscope, equipped with LAS-X version 4.8.2.29567 (Alvarez et al., 2019). The system was equipped with a stage-top incubator maintained at 37°C with 5% CO_2. As our sensor incorporates a tandem dark Venus acceptor, it allows capturing a large part of the donor emission spectrum while minimizing interference from acceptor emission. Detailed imaging settings is outlined in Table 1. The recorded TCSPC photon arrival time histograms and phasor plots showed multi-exponential decay, suggesting a superposition of (at least) two FRET states. Therefore, following acquisition, the photon arrival times were fitted to a double-exponential reconvolution function with fixed lifetimes τ_i of 0.6 ns and 3.4 ns, representing a high-FRET state and low-FRET state, respectively. They were exported from LAS X as *ImageJ TIF* files with 0.001 ns per gray value and used for downstream analysis and hit detection.

Imaging conditions	**Low responder screen**	**Baseline screen**
Lasers used	440 nm, 448 nm @ 40Mhz	440 nm, 448 nm @40Mhz
Detector(s)	HyDX2 for FLIM [460 nm – 552 nm]	HyDX2 for FLIM [460 nm – 552 nm]
Bidirectional scanning	Yes	Yes
Zoom	0.75	0.75
Pinhole	5.00	5.00
Scan format	512 x 512	512 x 512
Scan speed	400	400
Objective	20x 0.75 NA dry	20x 0.75 NA dry
Tiles (LASX Navigator)	240	304
Frames	10	2
Time resolution	6 minutes	6 minutes
Stimulation & Calibration	1 µM IsoP (Frame 2), 25 µM Forsk (Frame 8)	none
AFC used	Yes	Yes

Table 1 : *Imaging settings used for low responder and baseline screening*

DynaScreen (Low responders and Baseline screen) – Image analysis and hit detection

The exported tiles are stitched together using a Fiji script that in turn incorporates the Grid/Collection Stitching plugin (Preibisch *et al*, 2009) (Stitch_tiles macro; https://imagej.net/plugins/fast-hippos).

This is deliberately done without calculation of overlap in order to preserve stage positions. XY-Stage coordinates of image tiles are extracted from the OME metadata of the .lif file and stored in the metadata of the stitched .tif file, together with the grid layout, the tile size and the tile overlap percentage. The stitched image is then fed into the FAST-HIPPOS macro. Here, an output folder is outlined and cell segmentation and hit detection criteria are added. The analysis is performed directly after one hour of time-lapse imaging and took ~8 minutes for 240 tiles (2 seconds per 512x512 tile) for the low responder screen. For the baseline screen, the analysis is performed after 12 minutes of time-lapse imaging and took ~5 minutes for 304 tiles. The hit detection criteria in both screens are outlined below in Table 2. Among many output graphs and figures, the macro also generates a file with the stage coordinates of the hit cells (.rgn files in XML layout). This is then entered into LASX Navigator to start the photoactivation regime. Additionally, the lifetime traces generated by the macro are exported as .csv files and run through an R script for visualization and statistical analysis as detailed below.

Detailed step-by-step working of the macro is outlined in https://imagej.net/plugins/fast-hippos

	Low responder screen	**Baseline screen**
Image analysis – hit detection parameters	Response lifetime difference with the cell's own baseline in a 3 frame window should be lower than 0.4 ns + Baseline to calibration lifetime difference is more than 0.30 ns + Absolute baseline to average baseline difference is less than 0.30 ns	Baseline values > 2.6 ns

Table 2: *Hit detection criteria for the low responder and baseline screen*

DynaScreen (Low responders and Baseline screen) – Photoactivation of hit cells

Photoactivation of PA-Janelia-Fluor646 was with an external 355 nm pulsed laser (Spectra-Physics Explorer One 355-1) set at 50 kHz repetition rate, for 1.66 seconds per position with an average power of 1.7 µW. The laser beam was collimated by a 2-lens telescope system to a beam waist of ~5 mm at the back of the objective, thereby underfilling the backfocal plane. Additionally, the beam was slightly defocused, in such a way that the diameter of the spot in the sample plane was about 8 µm, slightly smaller than the size of a cell nucleus. The position of the focal plane was actively stabilized using the Leica Auto Focus Control (AFC) to prevent focal drift during photoactivation of multiple regions. Following photoactivation, Willco wells were stored in an incubator to maintain cell viability. Once imaging and photoactivation of all samples were complete, the samples were processed together for FACS. Samples with the PA-Janelia-Fluor646 dye were prepared and handled in the dark using aluminum foil to avoid background activation.

DynaScreen (Low responders and Baseline screen) – Preparing and FAC sorting hit cells

After trypsinization for FACS and treatment with trypsin inhibitor, cells were pelleted by centrifugation at 1400 rpm for 4 min, resuspended in FB medium, and passed through a polystyrene tube fitted with a cell-strainer cap (Corning) to obtain a single-cell suspension. Samples were kept on ice until sorting. Cell sorting was performed on a BD FACS Fusion cell sorter (BD Biosciences). Forward- and side-scatter parameters were used to exclude debris, doublets, and dead cells. Fluorescent signals were acquired using the following laser/filter combinations: PA-Janelia-Fluor646 was excited with a 532 nm laser and detected with a 610/20 nm filter; mVenus was excited at 488 nm and detected at 530/30 nm; and PA-Janelia-Fluor646 dye was excited with a 640 nm laser and detected at 670/30 nm.
Positive and negative controls were included for gating: positive controls consisted of cells photoactivated with a 395 nm LED, and negative controls were incubated with 1 µM dye but not photoactivated. The photoactivated cells of each replicate were sorted directly into PCR tubes containing the lysis buffer - DirectPCRlysis Reagent (Viagen).

DynaScreen (Low responders and Baseline screen) - Sequencing and sample preparation

Cells sorted into 20 µL of lysis mix (prepared by mixing 200 µL lysis buffer (Viagen), 200 µL Milli-Q water, and 2 µL Proteinase K (Viagen)) were first centrifuged at 1,100 rpm for 2 min. Lysis was performed using a thermal cycler: 3 h 15 min at 55 °C followed by 45 min at 80 °C to inactivate Proteinase K. Lysates were used directly in the first round of PCR (PCR1), with four parallel reactions per sample, each using 5 µL of lysate. PCR1 conditions are detailed in Table 3. A unique forward primer was used for each sample, optimized for LentiGuide templates (Supplementary File 3). This primer introduces an Illumina Read 1 sequencing adapter and a sample-specific barcode. The barcode allows us to index each sample separately and deconvolve the sequence reads after the pooled sequencing run. PCR1 products for each sample were pooled, and two replicate PCR2 reactions (5 µL input each) were performed to add flow cell adapters required for Illumina sequencing. PCR2 conditions are listed in Table 3. Together, the two rounds of PCR amplified the low DNA input to sufficient amounts for sequencing. To account for sample-to-sample variation in DNA yield, normalization was performed. A 10 µL aliquot of each PCR2 product was resolved on a 1% agarose gel to verify amplicon size and assess DNA quantity (Fig. S3B (i), (ii)). Band intensities were quantified to determine relative DNA concentrations and used to pool samples in defined ratios. The pooled sample was resolved again on a 1% agarose gel, and the desired product was excised and gel-purified. The final gel-purified product was submitted for next-generation sequencing.

PCR 1:	5 µL – Lysate 1 µL (10 µM) – FP 1 µL (10 µM) – RP 2 µL – MyTaq2Red 18 µL – milliQ Product size ~ 280 bp	98˚C – 30 s	98˚C – 30 s	60˚C – 30 s	72˚C – 1 min	72˚C – 5 min	Hold at 4˚C	35 cycles
PCR 2:	5 µL – PCR1 pooled product 1 µL (10 µM) – FP 1 µL (10 µM) – RP 25 µL – MyTaq2Red 18 µL – milliQ Product size ~ 350 bp	98˚C – 30 s	98˚C – 30 s	60˚C – 30 s	72˚C – 1 min	72˚C – 5 min	Hold at 4˚C	16 cycles

Table 3: *PCR1 and PCR2 conditions*

DynaScreen (Low responders and Baseline screen) - Bioinformatics analysis

With the NGS data, both CRISPR screens were analysed using the following approach: as a first step, we normalized sequence counts to account for variations in sequencing depth between samples. We implemented a normalization method analogous to that used by DESeq2 (Love *et al*, 2014) , but with an important adaptation. Specifically, we calculated a relative total size factor by taking the mean over all sample totals and dividing each sample total by this mean. Each count value within a sample was then divided by the corresponding size factor for that sample, resulting in equalized totals across all samples. We chose a size factor based on total counts rather than the median counts which DESeq2 uses, because some samples exhibited massive dropout in the sorted population, which would have resulted in a median value of zero for those samples, making normalization impossible.
The statistical analysis was performed in two sequential steps. First, we conducted a differential analysis between the sorted and reference populations using DESeq2, with the normalized counts as input, skipping the DESeq2 normalization step. Second, we performed an enrichment analysis on the gRNAs using MAGeCK's Robust Rank Algorithm (RRA) (Li *et al*, 2014b) using the results from the DESeq2 analysis as input. Because the RRA analysis in this case is about positive selection, we sorted the DESeq2 results on the DESeq2 test statistic from high to low. For the RRA analysis, we set the threshold for 'good gRNAs' (controlled by the maxPercentile parameter) based on our DESeq2 results. Specifically, we calculated this threshold as the percentage of gRNAs that showed both a positive test statistic (corresponding to a positive log2 fold change) and a p-value ≤ 0.25 relative to the total number of gRNAs in the dataset.

For hit selection, we used an FDR calculated by RRA ≤ 0.25 and a median log2 fold change ≥ 1 across all gRNAs targeting a gene. We selected this relaxed FDR threshold (rather than the more stringent 0.1) given the exploratory nature of these primary screens, allowing us to capture more potential hits for subsequent validation.

Hit validation

After obtaining the main and secondary hit gene names, validation experiments were performed for 14 genes in total:

ADRB2, **GNAS**, **ADCY6** - main hits of the low responder screen
PLCD4, AKAP11, SLC9A3R1, VPS26A, SNX13 – secondary hits of the low responder screen
RAPGEF3 – main hit of the baseline screen
SSTR1, RGS14, PDE1C, AP2A1, AP1G2 – secondary hits of the baseline screen

Monoclonal KO cell lines were made for the genes - ADRB2, GNAS and ADCY6 in HeLa cells. For the rest, polyclonal KO cell lines were made. Details of making a knockout cell line is outlined in Supplementary M&M. DNA was extracted from KO cell line and sequenced to confirm successful KO of the target genes. Following confirmation of gene KO, the cell lines were subjected to a microscopy assay to validate the phenotype. Low responder screen hits were stimulated with 1 µM isoproterenol and 25 µM forskolin and imaged for 1 hour (10 frames). Baseline screen hits were not stimulated and their baselines were recorded for 2 frames. The data was analysed using our Fiji analysis pipeline.

Statistical Analysis

A custom R script written in RStudio (version 2023.03.0) was used for data visualization (code available at Zenodo- https://doi.org/10.5281/zenodo.15827691). Briefly, the script runs through the .csv file which contains the lifetime data of every cell imaged per timepoint. Following determination of baseline lifetime values for each cell from the first 10 time points, the script allows setting criteria for inclusion of each individual cell based on outlier rejection and variance of time points within the baseline. Typically, between 1 and 15% of cells were rejected, often because of poor segmentation and/or detached cells that affect the validity of the data.
Since typical FOV contain up to 300 individual cells, we choose to plot the traces of 20 individual cells, picked randomly from all cells that pass inclusion criteria. To still fully capture the range and variability of the data, we also included a summary dotplot of the relevant data from all included cells, displayed next to the traces and at the same Y axis scale. Dotplots also show boxplots with median value (horizontal black line), middle 50% of values (boxes) and 1.5 times the interquartile range (whiskers). The datasets for all independent repeats are in the Zenodo data store.

Testing for statistical significance of relevant differences was carried out by unpaired one-tailed t-tests and one way ANOVA with multiple comparisons test where required and were all performed using GraphPad Prism (version 10.3). All statistical testing files are provided with the 'Analysed data' in Zenodo - https://doi.org/10.5281/zenodo.15827691. In the main text and legends, significances are marked as: ** $p < 0.05$; ** $p < 0.005$; *** $p < 0.0001$;* 'ns.' = not significant.

Data and software availability

All raw data sets, analysed data and R scripts are available on Zenodo repository - https://doi.org/10.5281/zenodo.15827691, unless mentioned otherwise.

FAST HIPPOS is available at: https://imagej.net/plugins/fast-hippos

ACKNOWLEDGMENTS

We are indebted to Dr. L. Bombardelli (Leiden University) and Dr. O. Kukk (Solis BioDyne) for insightful discussions and hands-on help during the initial phase of the project. We are grateful to Daniil Anastasopoulos (NKI, Amsterdam) for helping make the initial design of the H250 construct and Elke Malzer (NKI, Amsterdam) for all the support with downstream PCR processing. We are also grateful to the NKI FACS and Genomics facility for their technical support with all the experiments.

This study was supported by funding from NWO (TTW 14691 to K. Jalink). Research at the Netherlands Cancer Institute is supported by institutional grants of the Dutch Cancer Society and the Dutch Ministry of Health, Welfare and Sport. Part of the work has also been enabled by the European Union's Horizon Europe research innovation program under Marie Skłodowska-Curie Grant Agreement No. 101073507 (flIMAGIN3D – HORIZON-MSCA-DN-2021) and the NL-Bioimaging infrastructure sponsored by NWO National Roadmap for Large-Scale Research Infrastructure (NWO 184.036.012). Additional support was also received from ScreeninC Infrastructure (KWF 12539).

AUTHOR CONTRIBUTIONS

Conception of the study: K.J. and R.L.B.; design and execution of FLIM experiments: S.M. and K.J.; Designing of the library: S.M.; Generation of the library: R.L.B.; Sequencing of library and Dolcetto experiment: H.J.K. and S.M.; Optimization of HNS-PA-mCherry: S.M. and K.J.; Optimization of the PA-Janelia-Fluor646 – M.v.T., S.M., B.vd.B. and K.J.; Screens: S.M., D.S. and D.K.; Validation of hits from screens: G.Z., D.K. and S.M.; Bioinformatics analysis of NGS data: C.L.; preparation of molecular constructs, construction of stable cell lines, and cell culturing: S.M., J.K., G.Z., D.K. and M.v.T; ImageJ scripts for automatic cell segmentation, extraction of single-cell FLIM traces and hit identification: B.vd.B., K.J. and S.M.; data analysis, statistics, and preparation of figures: S.M., K.J. and B.vd.B.; R scripts for data visualization: S.M. and K.J.; ELISA assays: S.M.; preparation of the manuscript: S.M. and K.J. All authors provided critical input during finalizing of the manuscript.

DECLARATION OF INTERESTS

The authors declare no conflicting interests.

REFERENCES

Albeck JG, Mills GB & Brugge JS (2013) Frequency-Modulated Pulses of ERK Activity Transmit Quantitative Proliferation Signals. *Molecular Cell* 49: 249–261

Alvarez LAJ, Widzgowski B, Ossato G, van den Broek B, Jalink K, Kuschel L, et al. SP8 FALCON: A novel concept in fluorescence lifetime imaging enabling video-rate confocal FLIM. Application Note. Leica Microsystems; 2019.

Azevedo MF, Faucz FR, Bimpaki E, Horvath A, Levy I, de Alexandre RB, Ahmad F, Manganiello V & Stratakis CA (2014) Clinical and Molecular Genetics of the Phosphodiesterases (PDEs). *Endocr Rev* 35: 195–233

Ben-Shlomo A, Wawrowsky K & Melmed S (2010) Chapter Eight - Constitutive Activity of Somatostatin Receptor Subtypes. In *Methods in Enzymology*, Conn PM (ed) pp 149–164. Academic Press

Bernatchez R, Belkacemi L, Rassart E, Daoud G, Simoneau L & Lafond J (2003) Differential Expression of Membrane and Soluble Adenylyl Cyclase Isoforms in Cytotrophoblast Cells and Syncytiotrophoblasts of Human Placenta. *Placenta* 24: 648–657

Bock C, Datlinger P, Chardon F, Coelho MA, Dong MB, Lawson KA, Lu T, Maroc L, Norman TM, Song B, *et al* (2022) High-content CRISPR screening. *Nat Rev Methods Primers* 2: 8

Ding H, Zhang X, Su Y, Jia C & Dai C (2020) GNAS promotes inflammation-related hepatocellular carcinoma progression by promoting STAT3 activation. *Cellular & Molecular Biology Letters* 25: 8

Doench JG, Fusi N, Sullender M, Hegde M, Vaimberg EW, Donovan KF, Smith I, Tothova Z, Wilen C, Orchard R, *et al* (2016) Optimized sgRNA design to maximize activity and minimize off-target effects of CRISPR-Cas9. *Nat Biotechnol* 34: 184–191

Donnelly MLL, Hughes LE, Luke G, Mendoza H, Ten Dam E, Gani D & Ryan MD (2001) The 'cleavage' activities of foot-and-mouth disease virus 2A site-directed mutants and naturally occurring '2A-like' sequences. *J Gen Virol* 82: 1027–1041

Fan XC & Steitz JA (1998) HNS, a nuclear-cytoplasmic shuttling sequence in HuR. *Proc Natl Acad Sci U S A* 95: 15293–15298

Feldman D, Singh A, Schmid-Burgk JL, Carlson RJ, Mezger A, Garrity AJ, Zhang F & Blainey PC (2019) Optical Pooled Screens in Human Cells. *Cell* 179: 787-799.e17

Haase R, Royer LA, Steinbach P, Schmidt D, Dibrov A, Schmidt U, Weigert M, Maghelli N, Tomancak P, Jug F, *et al* (2020) CLIJ: GPU-accelerated image processing for everyone. *Nat Methods* 17: 5–6

Harkes R, Kukk O, Mukherjee S, Klarenbeek J, van den Broek B & Jalink K (2021) Dynamic FRET-FLIM based screening of signal transduction pathways. *Sci Rep* 11: 20711

Hasle N, Cooke A, Srivatsan S, Huang H, Stephany JJ, Krieger Z, Jackson D, Tang W, Pendyala S, Monnat RJ, *et al* (2020) High-throughput, microscope-based sorting to dissect cellular heterogeneity. *Molecular Systems Biology* 16: e9442

He MY, Tong KI, Liu T, Whittaker Hawkins R, Shelton V, Zeng Y, Bakhtiari M, Xiao Y, Zheng G, Sakhdari A, *et al* (2024) GNAS knockout potentiates HDAC3 inhibition through viral mimicry-related interferon responses in lymphoma. *Leukemia* 38: 2210–2224

Henne WM, Zhu L, Balogi Z, Stefan C, Pleiss JA & Emr SD (2015) Mdm1/Snx13 is a novel ER–endolysosomal interorganelle tethering protein. *Journal of Cell Biology* 210: 541–551

Inda C, Bonfiglio JJ, dos Santos Claro PA, Senin SA, Armando NG, Deussing JM & Silberstein S (2017) cAMP-dependent cell differentiation triggered by activated CRHR1 in hippocampal neuronal cells. *Sci Rep* 7: 1944

Kanfer G, Sarraf SA, Maman Y, Baldwin H, Dominguez-Martin E, Johnson KR, Ward ME, Kampmann M, Lippincott-Schwartz J & Youle RJ (2021) Image-based pooled whole-genome CRISPRi screening for subcellular phenotypes. *Journal of Cell Biology* 220: e202006180

Kawaguchi S, Nagasaki N & Hirano T (2011) Dynamic impact of temporal context of Ca2+ signals on inhibitory synaptic plasticity. *Sci Rep* 1: 143

Kawakami K (2007) Tol2: a versatile gene transfer vector in vertebrates. *Genome Biology* 8: S7

Kim CS, Cairns J, Quarantotti V, Kaczkowski B, Wang Y, Konings P & Zhang X (2024) A statistical simulation model to guide the choices of analytical methods in arrayed CRISPR screen experiments. *PLoS One* 19: e0307445

Klarenbeek J, Goedhart J, Batenburg A van, Groenewald D & Jalink K (2015) Fourth-Generation Epac-Based FRET Sensors for cAMP Feature Exceptional Brightness, Photostability and Dynamic Range: Characterization of Dedicated Sensors for FLIM, for Ratiometry and with High Affinity. *PLOS ONE* 10: e0122513

Klarenbeek JB, Goedhart J, Hink MA, Gadella TWJ & Jalink K (2011) A mTurquoise-Based cAMP Sensor for Both FLIM and Ratiometric Read-Out Has Improved Dynamic Range. *PLOS ONE* 6: e19170

Lawson MJ, Camsund D, Larsson J, Baltekin Ö, Fange D & Elf J (2017) In situ genotyping of a pooled strain library after characterizing complex phenotypes. *Molecular Systems Biology* 13: 947

Li HL, Verhoeven A & Elferink RO (2024) The role of soluble adenylyl cyclase in sensing and regulating intracellular pH. *Pflugers Arch - Eur J Physiol* 476: 457–465

Li J, Li C, Zhang D, Shi D, Qi M, Feng J, Yuan T, Xu X, Liang D, Xu L, *et al* (2014a) SNX13 reduction mediates heart failure through degradative sorting of apoptosis repressor with caspase recruitment domain. *Nat Commun* 5: 5177

Li W, Xu H, Xiao T, Cong L, Love MI, Zhang F, Irizarry RA, Liu JS, Brown M & Liu XS (2014b) MAGeCK enables robust identification of essential genes from genome-scale CRISPR/Cas9 knockout screens. *Genome Biology* 15: 554

Love MI, Huber W & Anders S (2014) Moderated estimation of fold change and dispersion for RNA-seq data with DESeq2. *Genome Biology* 15: 550

Massengill CI, Day-Cooney J, Mao T & Zhong H (2021) Genetically encoded sensors towards imaging cAMP and PKA activity *in vivo*. *Journal of Neuroscience Methods* 362: 109298

Mukherjee S, Klarenbeek J, Oualid FE, Broek B van den & Jalink K (2024) “Radical” differences between two FLIM microscopes affect interpretation of cell signaling dynamics. *iScience* 27

Pachitariu M & Stringer C (2022) Cellpose 2.0: how to train your own model. *Nat Methods* 19: 1634–1641

Piatkevich KD, Jung EE, Straub C, Linghu C, Park D, Suk H-J, Hochbaum DR, Goodwin D, Pnevmatikakis E, Pak N, *et al* (2018) A robotic multidimensional directed evolution approach applied to fluorescent voltage reporters. *Nat Chem Biol* 14: 352–360

Pontén F, Jirström K & Uhlen M (2008) The Human Protein Atlas—a tool for pathology. *The Journal of Pathology* 216: 387–393

Pratt EPS, Harvey KE, Salyer AE & Hockerman GH (2019) Regulation of cAMP accumulation and activity by distinct phosphodiesterase subtypes in INS-1 cells and human pancreatic β-cells. *PLOS ONE* 14: e0215188

Preibisch S, Saalfeld S & Tomancak P (2009) Globally optimal stitching of tiled 3D microscopic image acquisitions. *Bioinformatics* 25: 1463–1465

Reicher A, Reiniš J, Ciobanu M, Růžička P, Malik M, Siklos M, Kartysh V, Tomek T, Koren A, Rendeiro AF, *et al* (2024) Pooled multicolour tagging for visualizing subcellular protein dynamics. *Nat Cell Biol* 26: 745–756

RStudio Team. *RStudio: Integrated Development Environment for R*. Posit, PBC, https://www.posit.co/ (2023).

R Core Team. *R: A language and environment for statistical computing*. R Foundation for Statistical Computing, https://www.R-project.org/ (2023).

Sanson KR, Hanna RE, Hegde M, Donovan KF, Strand C, Sullender ME, Vaimberg EW, Goodale A, Root DE, Piccioni F, *et al* (2018) Optimized libraries for CRISPR-Cas9 genetic screens with multiple modalities. *Nat Commun* 9: 5416

Schindelin J, Arganda-Carreras I, Frise E, Kaynig V, Longair M, Pietzsch T, Preibisch S, Rueden C, Saalfeld S, Schmid B, *et al* (2012) Fiji: an open-source platform for biological-image analysis. *Nat Methods* 9: 676–682

Seaman MNJ (2012) The retromer complex – endosomal protein recycling and beyond. *Journal of Cell Science* 125: 4693–4702

Shi H, Rojas R, Bonifacino JS & Hurley JH (2006) The retromer subunit Vps26 has an arrestin fold and binds Vps35 through its C-terminal domain. *Nat Struct Mol Biol* 13: 540–548

Simko V, Iuliano F, Sevcikova A, Labudova M, Barathova M, Radvak P, Pastorekova S, Pastorek J & Csaderova L (2017) Hypoxia induces cancer-associated cAMP/PKA signalling through HIF-mediated transcriptional control of adenylyl cyclases VI and VII. *Sci Rep* 7: 10121

Stringer C, Wang T, Michaelos M & Pachitariu M (2021) Cellpose: a generalist algorithm for cellular segmentation. *Nat Methods* 18: 100–106

Tian G, Sandler S, Gylfe E & Tengholm A (2011) Glucose- and hormone-induced cAMP oscillations in α- and β-cells within intact pancreatic islets. *Diabetes* 60: 1535–1543

Walton RT, Singh A & Blainey PC (2022) Pooled genetic screens with image-based profiling. *Molecular Systems Biology* 18: e10768

Wang C, Lu T, Emanuel G, Babcock HP & Zhuang X (2019) Imaging-based pooled CRISPR screening reveals regulators of lncRNA localization. *Proceedings of the National Academy of Sciences* 116: 10842–10851

Wang J, Guo Y, He Y, Qin Y, Li X, Yang L, Liu K & Xiao L (2024) Hepatic regulator of G protein signaling 14 ameliorates NAFLD through activating cAMP-AMPK signaling by targeting Giα1/3. *Mol Metab* 80: 101882

Wheeler EC, Vu AQ, Einstein JM, DiSalvo M, Ahmed N, Van Nostrand EL, Shishkin AA, Jin W, Allbritton NL & Yeo GW (2020) Pooled CRISPR screens with imaging on microraft arrays reveals stress granule-regulatory factors. *Nat Methods* 17: 636–642

Yan X, Stuurman N, Ribeiro SA, Tanenbaum ME, Horlbeck MA, Liem CR, Jost M, Weissman JS & Vale RD (2021) High-content imaging-based pooled CRISPR screens in mammalian cells. *Journal of Cell Biology* 220: e202008158

Zanetti G, Klarenbeek JB & Jalink K (2025) Cytosolic-enhanced dark Epac-based FRET sensors allow for intracellular cAMP detection in live cells via FLIM. *FEBS Letters* 599: 1075–1085

Zhang T, Du J, Liu L, Chen X, Yang F & Jin Q (2012) Inhibitory Effects and Underlying Mechanism of 7-Hydroxyflavone Phosphate Ester in HeLa Cells. *PLOS ONE* 7: e36652

Zheng B, Tang T, Tang N, Kudlicka K, Ohtsubo K, Ma P, Marth JD, Farquhar MG & Lehtonen E (2006) Essential role of RGS-PX1/sorting nexin 13 in mouse development and regulation of endocytosis dynamics. *Proceedings of the National Academy of Sciences* 103: 16776–16781